

October 17, 1999

Robert S. Nelson  
2922 Upshur Street  
San Diego, CA 92106

Disclosed Invention:

Device and Method for Improved Imaging in Nuclear Medicine  
-----

Nuclear medicine imaging represents a challenge since the energies utilized are relatively high in comparison to Diagnostic Radiology requirements and the radiation source (radionuclides) is not directional and its distribution within the body is not precisely known. An extreme example is PET (Positron Emission Tomography) which involves very high energies. Emitted radiation which escapes the body can be scattered which can alter its direction and energy. It is desirable (in most cases) to reject scatter radiation reaching the detector based on energy and/or direction.

Most imaging systems used in Nuclear Medicine imaging are based on the Gamma camera design (a large scintillation crystal or array of scintillation crystals optically coupled to an array of Photo Multiplier Tubes (PMTs). Depending upon the imaging task, a flat or focused collimator is located between the Gamma camera and the object. This system provides a limited degree of spatial resolution and energy resolution while removing some fraction of the scatter radiation which would otherwise degrade image quality and diagnosis. Current systems use 1, 2, or 3 Gamma cameras detector units. At least one commercial system eliminates the use of scintillator crystals and PMTs with a semiconductor detector (CdZnTe) manufactured into a 2-D array. Drawbacks include the difficulty of growing large area, thick CdZnTe crystals which have problems with defects and forming a low noise, 2-D readout structure on a CdZnTe crystal. Grid collimation is still desirable for many applications. ('DigiRad', San Diego, CA 92126, 858-578-5300). Yet another design which avoids the use of a collimator (basically replacing it with a thin semiconductor which plays the role of a Compton scatter) can be thought of as a Compton Gamma camera. This design is not used commercially.

A new Gamma camera design utilizes the concept of edge-on detectors as described by Nelson in patent 4,937,453. Manufacturing requirements in comparison to large area, thick, 2-D semiconductor arrays from CdZnTe, CdTe, GaAs, Ge, Si, SiC, HgI<sub>2</sub>, etc. are greatly reduced. Because radiation is incident on the edge of the detector the thickness of the detector now represents the maximum entrance aperture while the length or width of the detector area now represents the maximum attenuation distance for radiation. Drift and single-sided or double-side strip detectors configurations can be implemented depending on the semiconductor material chosen. Strip widths can be tapered (or curved in the case of drift detectors) if focusing is desired. In the case of double-sided strip detectors electrons and holes can be collected to provide 2-D position information across the aperture or depth of interaction information can

be acquired.

Nelson has shown in patent 4,937,453 how large area 2-D detectors can be formed by the close proximity of multiple edge-on linear detector arrays. (See FIG. 1.) Limited focusing, in the case of strip detectors, is possible by tapering the strips for each linear array. Of course, a slat or focused grid can still be used with this design. Alternative geometric configurations may also be implemented other than a planar array (a conventional format). FIG. 2a and FIG. 3 show arrays of edge-on detectors used in focused cylindrical and spherical lens-like geometries. It is obvious that these configurations can be "filled-out" to form complete cylinders (rings) or nearly-complete spherical detector arrays. Collimation can be provided for individual edge-on detectors (FIG. 2b) and shielding can be used as needed to minimize radiation escaping from neighboring detectors. The entire detector array mount can be moved as can individual edge-on detectors within the array. This allows the detector array to be refocused as needed or to reposition individual edge-on detectors in order to optimize its field of view for the specific distribution of radionuclide. The entire array or individual edge-on detectors can be dithered to provide appropriate sampling of spatial regions which would otherwise be 'dead areas' due to a lack of detectors at those positions. Alternatives to conventional collimation (which may also be used to expand the aperture of an edge-on detector and energy resolution) are the use of one or more of reflective x-ray mirrors or Bragg crystals, capillary x-ray optics, or refractive x-ray lenses. A combination of a x-ray mirror or Bragg crystal with a minifying capillary x-ray optic is shown in FIG. 4. The use of such devices must take into consideration the energy of the radiation and the physical size limitations of the (edge-on) Gamma Camera.

Although this device and method have been described in terms of use for Nuclear Medicine, it is clear that industrial/scientific applications could also benefit. In addition, radiological applications such as Compton scatter imaging will also benefit from this design.

Cooling of the edge-on detectors may be implemented as needed. Preferably the detectors will operate at or near room temperature for applications in Nuclear Medicine, but this may not always be possible. In some instances heating may be needed depending upon the detector package and the operational environment.

October 17, 1999

Robert S. Nelson  
2922 Upshur Street  
San Diego, CA 92106

Disclosed Invention:

Device and Method for Improved Scanned Mammography  
-----

Development goals for x-ray mammography imaging systems include high detectivity of disease conditions with minimal acceptable risk to the patient. Numerous efforts have been made or are underway to replace standard x-ray film-screen detectors with digital detectors. These digital detectors can have geometries which vary from slits and slots (which provide a level of self-collimation) to flat plates or 2-D detector arrays (which typically use a grid depending on the size of the breast being imaged). Slit and slot devices are scanned across a stationary, compressed breast and thereby acquiring a single continuous image (the same format which is acquired when using film-screen or plate/2-D digital detectors).

Advantages which digital detectors may hold over analog film-screen detectors include an extended dynamic range, superior detection efficiency, and the option of easy use of post-processing of the image. In some instances the contrast resolution of the digital detector may exceed that of the film-screen unit over the frequency range of interest.

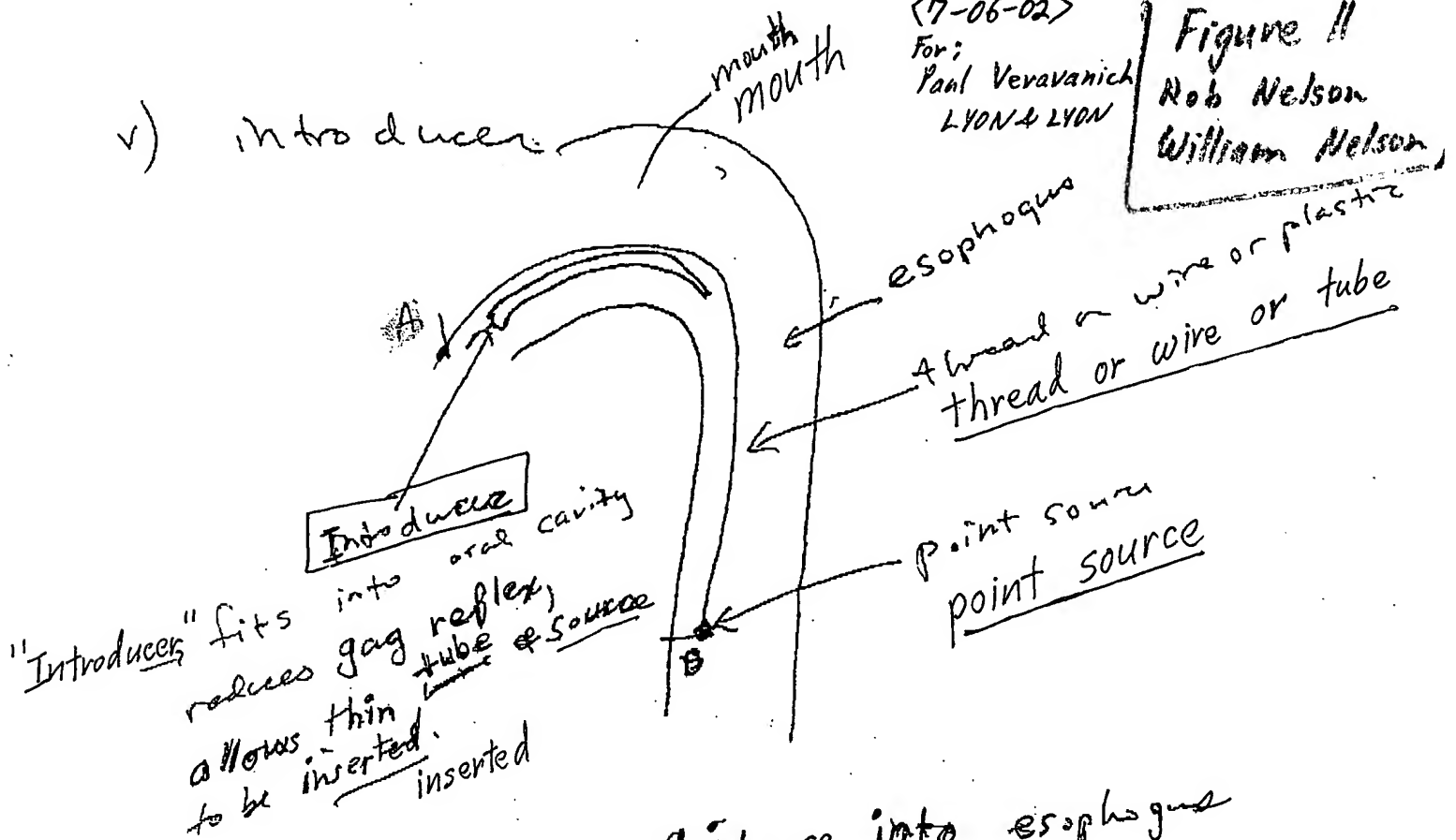
Other aspects of the imaging chain can be optimized to further improve the final image. For example, the x-ray beam spectrum in a slit or slot format can be filtered using a variety of techniques (capillary optics, refractive lenses, multilayer mirrors or Bragg crystal spectrometers) or combinations thereof (see FIG. 3). If the detector itself is capable of providing energy resolution, this could be used to improve contrast or reject a fraction of the incident scattered x-rays. The variable magnification from center-to-edge of the beam could be corrected with appropriate x-ray optics. This would reduce the problem of depth-dependent magnification for objects positioned at different locations within the breast. In addition, the x-ray optics may be used to focus the x-ray beam, thus increasing the intensity for a slit or slot scan format and thereby reducing the power requirement for the x-ray tube.

Slit or slot scanning techniques are typically much more efficient at reducing the level of scattered x-rays reaching the detector (which reduces contrast resolution). If slit or slot scanning is implemented such that the scanning speed minimizes the effects of patient motion (blurring) on contrast resolution of the local image then there may not be a need to acquire the entire image in a single, continuous pass of the scanning system. This suggests that greater local compression of the breast can be acceptable. The benefits include reduced x-ray tube heat loading (lower instantaneous power requirements), reduced scatter, reduced x-ray attenuation and filtration. Greater local compression can be attained using compression

plates which are reduced in size. This can be attained using flat, contoured, or sliding compression plates (See Nelson and Zach, patent serial number 08/597,447 and pending CIP) as shown in FIG. 1a, 1b. Image acquisition then involves acquiring a number of sub-images (with suitable overlap) which can be viewed separately or assembled into a larger image (see FIG. 2). Overall scanning times will increase, but this should not be an issue since image acquisition times for current systems are very short.

(v) capsule may be  
and held in place in a magnetic field.

v) introducer

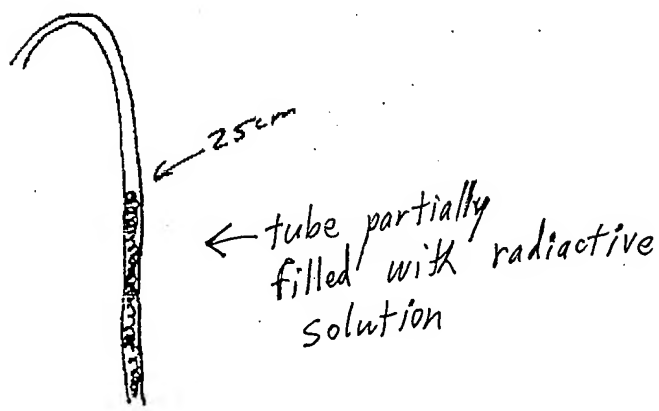
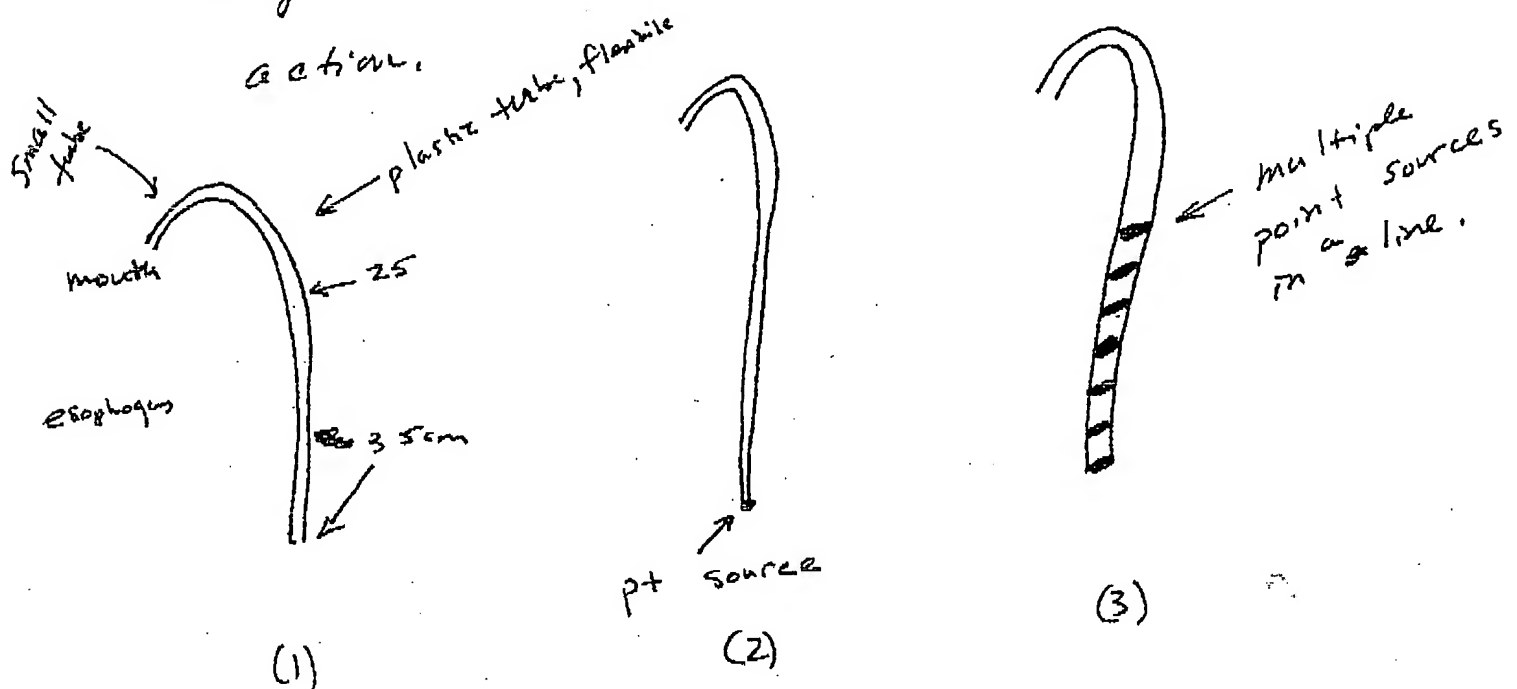


wire/source inserted similar to N6 tube  
over introducer but ~~not~~ <sup>plastic</sup> wire/source ~~much~~  
smaller than N6. tube. Could also be  
introduced nasally.

Vii) solution that is radioactive & binds  
to esophagus (coats esophagus) - gives essentially  
a line source.

examples:

a thin plastic tube, flexible, possible coated with radioactive material, or beads, or point source at tip. Another method would be to draw solution of radioactive material e.g. thallium into tube via capillary action.



Solution of radioactive material of known activity taken up by capillary action from solution.

Figure 11

Rob Nelson

William Nelson

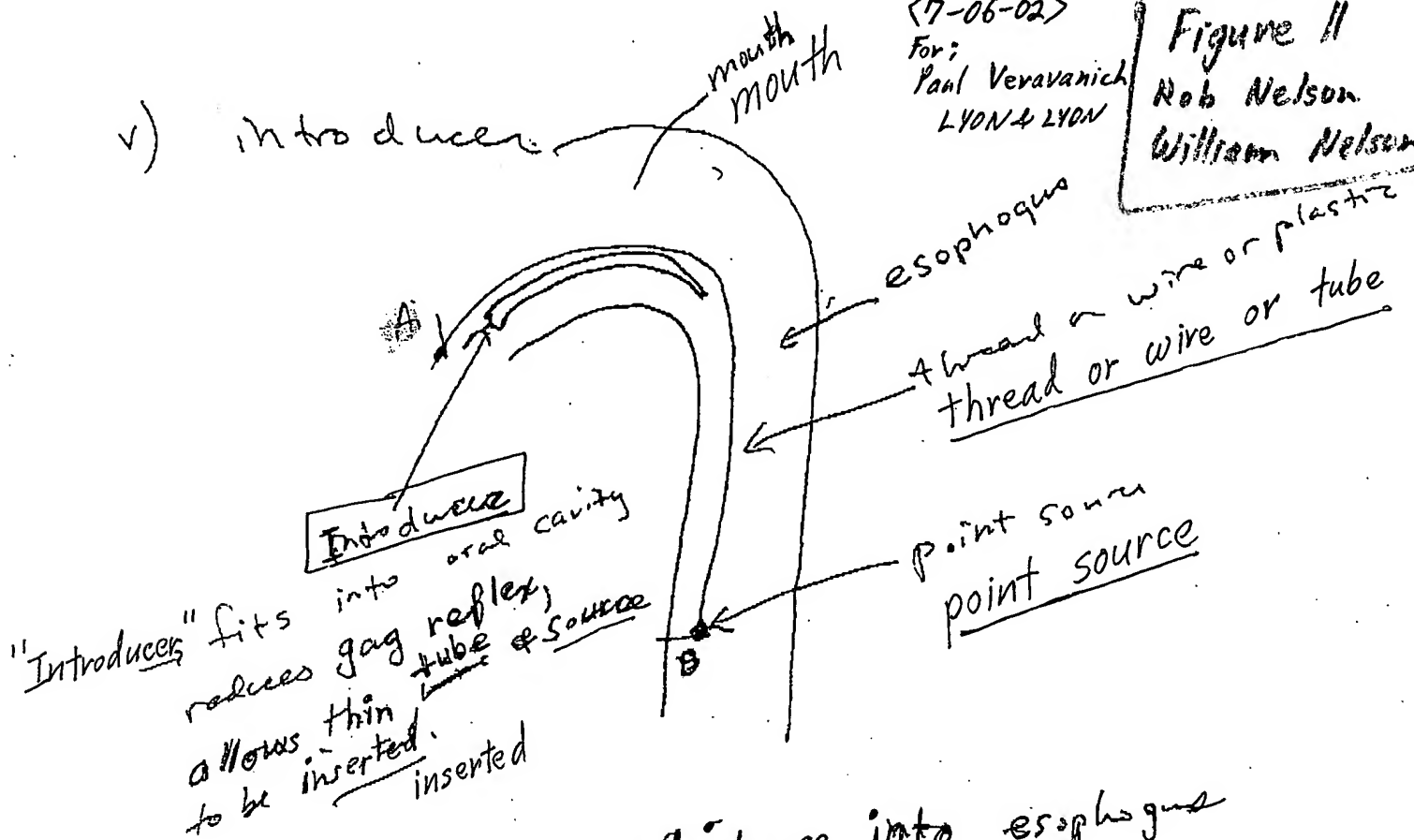
(v) capsule may be magnetic / paramagnetic and held in place in a magnetic field.

v) introducer

(7-06-02)

For:  
Paul Veravanich  
LYON & LYON

Figure II  
Rob Nelson  
William Nelson



A → B = distance into esophagus  
25-35 cm.

wire / source inserted similar to N6 tube  
over introducer but ~~no~~ <sup>plastic</sup> / wire / source ~~much~~  
smaller than N6. tube. Could also be  
introduced nasally.

Vii) solution that is radioactive & binds  
to esophagus (coats esophagus) - gives essentially  
a line source.

examples:

a thin plastic tube, flexible, possibly coated with radioactive material, or beads, or point source at tip. Another method would be to draw solution of radioactive material e.g. thallium into tube via capillary action.

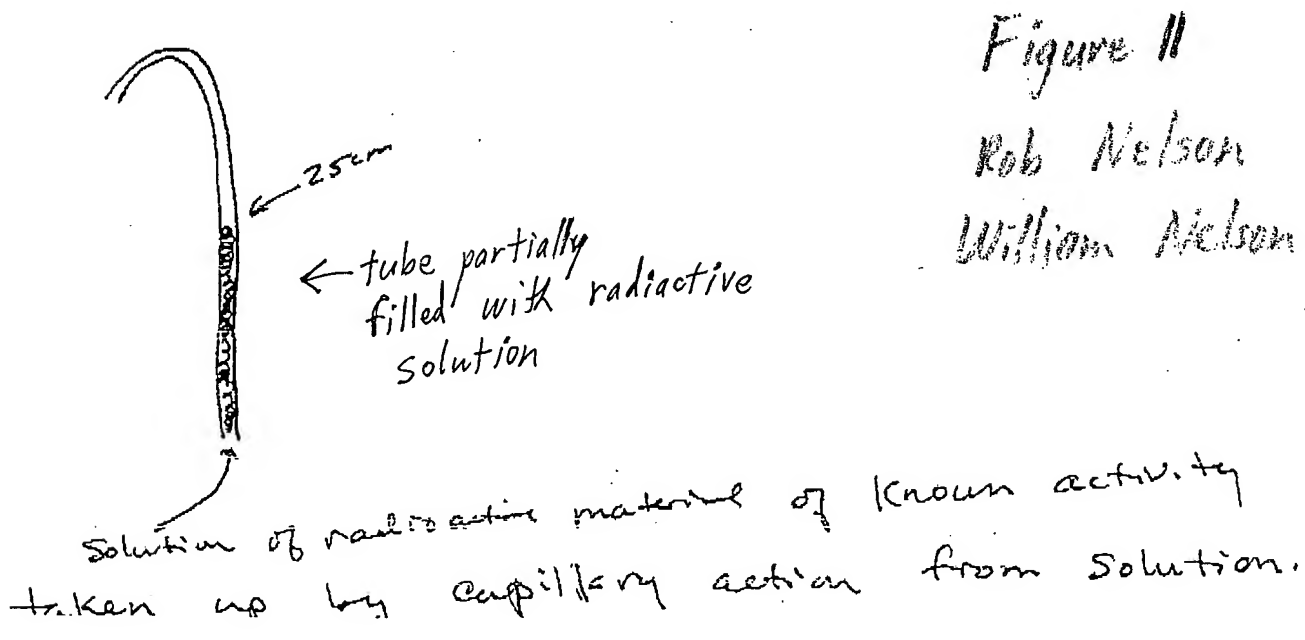
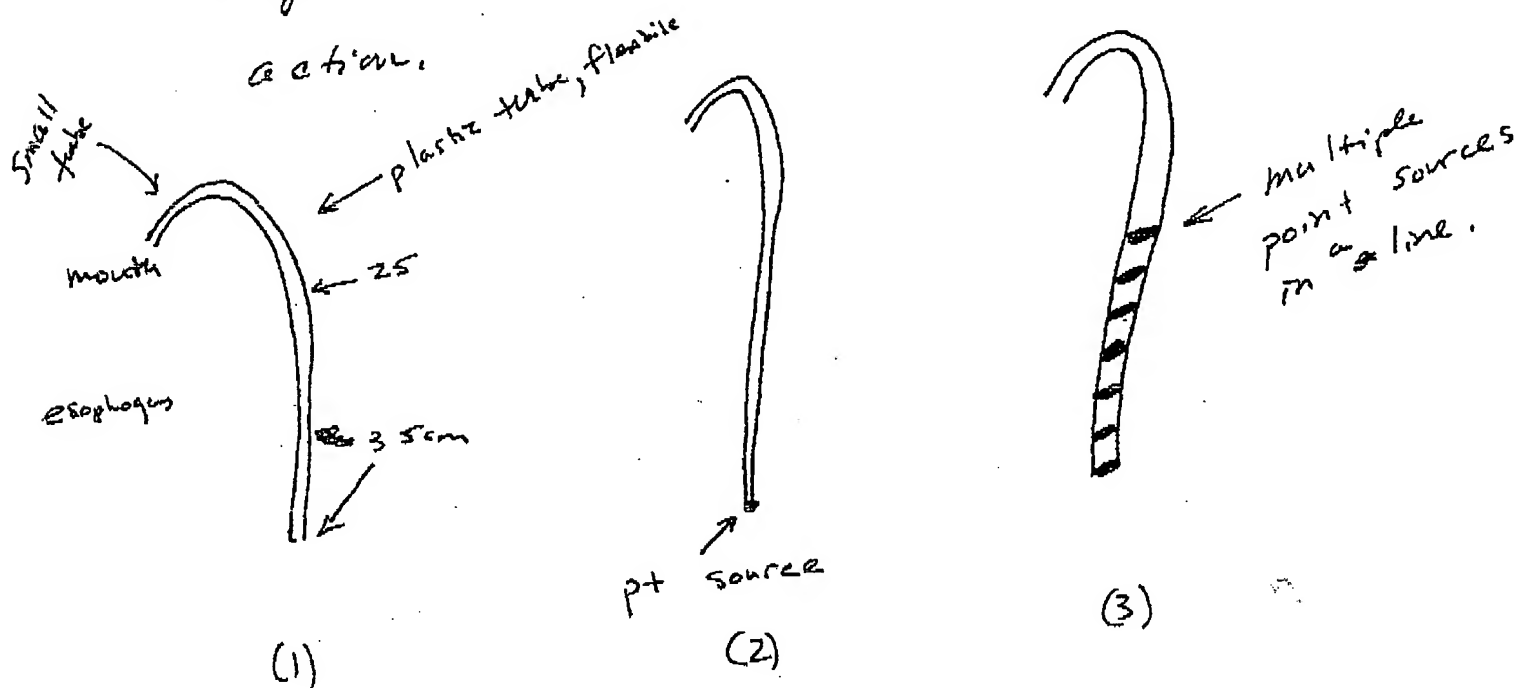


Figure 11

Rob Nelson

William Nelson



To: Box DD  
Commissioner for Patents  
Washington, DC 20231

From: Robert S. Nelson  
2922 Upshur Street  
San Diego, CA 92106

Disclosure Document

Inventors: Robert Sigurd Nelson, William Bert Nelson  
Title of Invention: Device and Method for Improved Compton Imaging  
Date: June 2, 2002

Description:

Compton cameras typically consist of a Compton scattering device such as a thin semiconductor array aligned with (and typically separate from) a thicker detector. A pending application titled "Device and System for Improved Imaging in Nuclear Medicine and Mammography" describes an implementation that includes such a thin array used with an edge-on or strip detector array -based Gamma Camera. This is a traditional format for a Compton Gamma camera.

Now consider that our edge-on (or strip) detector has sufficient spatial resolution so that an event (photoabsorption or scattering) occurring within a detector element can be localized. This can be achieved by making the edge-on detector into a pixilated array or by having crossed-readout stripes on opposite sides of the edge-on detector. Migration times for holes and electrons can be used to localize the event with respect to the two sides. There are a number of configurations such that the edge-on or strip detector array can function as a Compton camera:

1. The semiconductor edge-on (or strip) detectors act as both Compton scatterers and Compton scatter detectors. (See Fig. 1.)
2. The semiconductor edge-on (or strip) detectors are constructed from a stack of edge-on (or strip) detectors made from different materials. One material may be selected as the Compton scatter based on a high likelihood that for appropriate photon energies scattering dominates absorption. The second material may be selected such that absorption dominates scatter. We are not limited to using only two materials, the idea is easily extended to use 3, 4, ... materials. (See Fig. 2.)
3. Alternate semiconductor edge-on (or strip) detector materials within an array configuration. The materials can be selected using the criteria described in configuration 2. (See Fig. 3.)

Configurations 2 and 3 may be more complex to implement than configuration 1 but may improve Compton imaging efficiency relative to configuration 1. All 3 configurations may be used for conventional imaging.

To: Box DD  
Commissioner for Patents  
Washington, DC 20231

From: Robert S. Nelson  
2922 Upshur Street  
San Diego, CA 92106

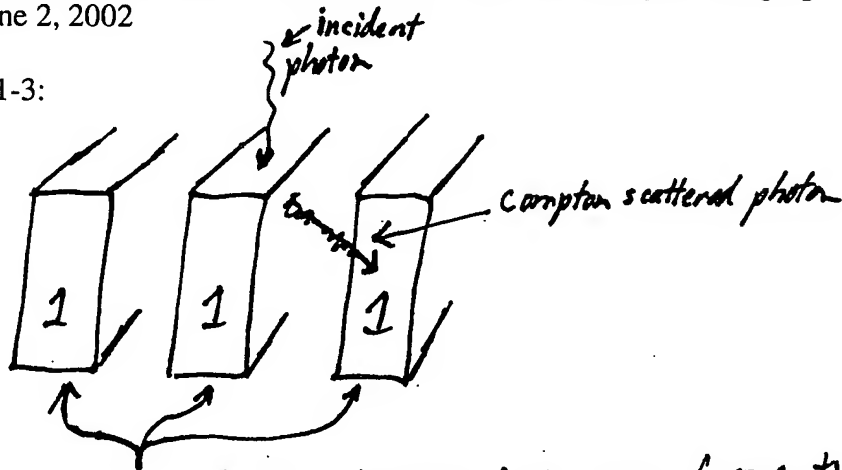
Disclosure Document

Inventors: Robert Sigurd Nelson, William Bert Nelson  
Title of Invention: Device and Method for Improved Compton Imaging  
Date: June 2, 2002

Figures 1-3:

R.S. Nelson  
6-02-02

Figure 1



Edge-on semiconductor detector (all are of one type s.a. Si, Ge, CdZTe, CdTe, SiC, etc.,

Figure 2

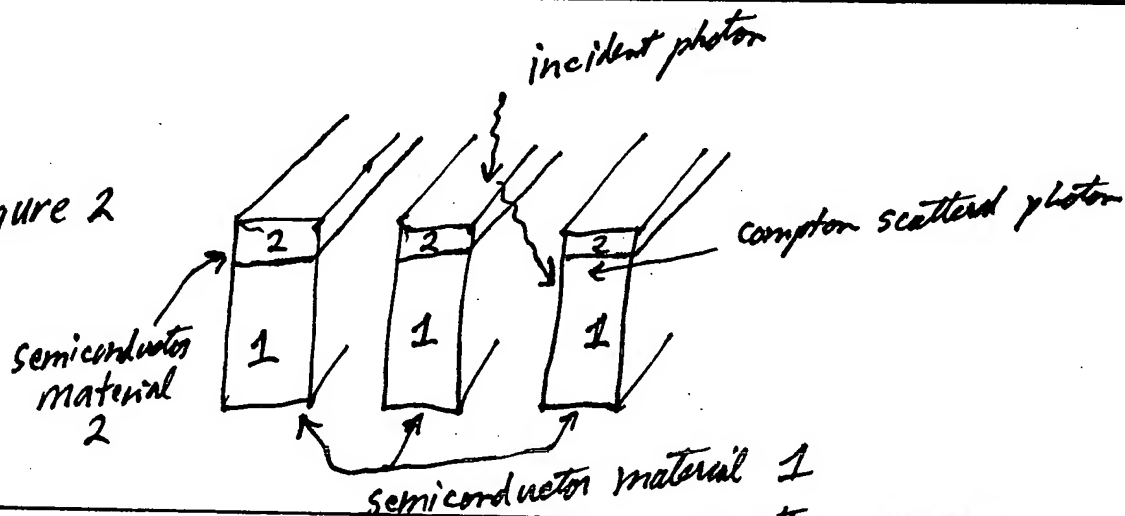
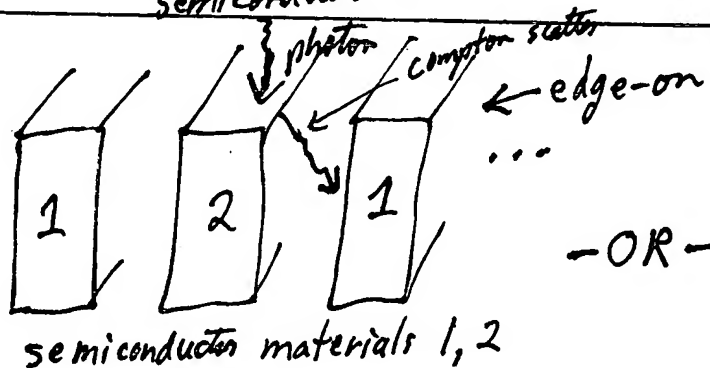
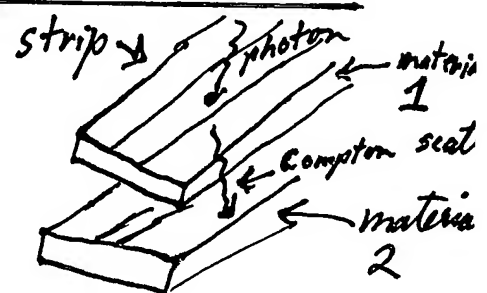


Figure 3



-OR-



# Model calculations of the response of CZT strip detectors

E. Kalemci<sup>a</sup>, J. L. Matteson<sup>a</sup>, R. T. Skelton<sup>a</sup>  
P. L. Hink<sup>b</sup> and K. R. Slavis<sup>b</sup>

<sup>a</sup>Center for Astrophysics and Space Sciences, University of California  
San Diego  
9500 Gilman Dr., La Jolla, CA 92093-0424

<sup>b</sup>Department of Physics and McDonnell Center for the Space Sciences  
Washington University  
St. Louis, MO 63130

## ABSTRACT

Position-sensitive CZT detectors for research in astrophysics in the five – several hundred keV range are being developed by several groups. These are very promising for large area detector arrays in coded mask imagers and small-area focal plane detectors for focusing X-ray telescopes. We have developed detectors with crossed-strip readout and optimized strip widths and gaps to improve energy resolution. A “steering electrode” is employed between the anode strips to improve charge collection. A model of charge drift in the detectors and charge induction on the electrodes has been developed to allow us to better understand these types of detectors and improve their design. The model presently accounts for the electric field within the detector, the charges’ trajectories, mobility and trapping of holes and electrons, and charge induction on all electrodes including their time dependence. Additional effects are being added. The model is described and its predictions are compared with laboratory measurements. Results include (1) the dependence of anode, cathode and steering electrode signals on interaction depth, transverse (to the strips) position, electron and hole trapping, strip width and gap, and bias, (2) trajectories of charges for various anode and steering electrode bias voltages, (3) a method to improve energy resolution by using depth of interaction information, and (4) an electrode geometry and bias optimized for the improved energy resolution. In general, the model provides good agreement with the measurements.

**Keywords:** CdZnTe, CZT detectors, strip detectors, solid state detectors, X-ray astronomy

## 1. INTRODUCTION

CdZnTe (CZT), a semiconductor detector of X-rays and gamma-rays, has numerous applications in scientific and technological fields, most notably in medical imaging and high energy astrophysics. An important objective of high energy X-ray astronomy is a full sky survey at energies  $\sim 10$  to several hundred keV at a sensitivity level that will yield many new sources.<sup>1</sup> These sources include ordinary objects such as stellar coronea, galaxies, cluster of galaxies as well as exotic ones, such as black holes, active galactic nuclei and neutron stars. Fundamental information on many topics in astrophysics is obtained by observing those sources in X-rays. Coded mask techniques can be used along with a detector having submillimeter position resolution and a few keV energy resolution to achieve this objective.<sup>2</sup> (For more information on the objectives and status of high energy astronomy, see Matteson et al.<sup>3</sup>)

These requirements are met with CZT. It is dominated by photoelectric absorption due to high Z, and its large bandgap ( $\sim 1.4$  eV) allows room temperature operation. Its high bulk resistivity at room temperatures,  $\sim 10^{11}$   $\Omega$ cm, results in low leakage currents and noise in a small detector, i.e. 1 cm<sup>2</sup>. CZT’s energy response is linear over the energy range of interest.<sup>4</sup> However, CZT material has poor hole transport properties. Conventional planar configuration for the detector shows low energy tailing in their spectra for energies higher than 60 keV due to incomplete hole collection. Strip or pixel detectors can eliminate this problem by virtue of the small pixel effect.<sup>5,6</sup>

Further author information:

E. Kalemci: E-mail: emrahk@mamacass.ucsd.edu

J. L. Matteson: E-mail: jmatteson@ucsd.edu

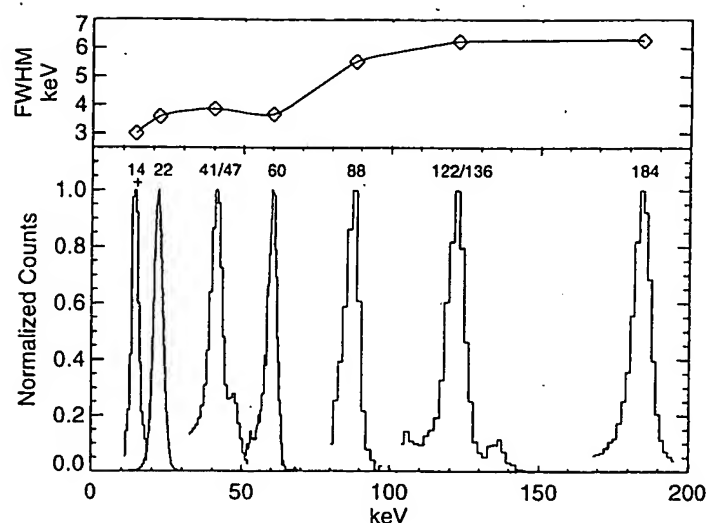


Figure 1. Line profiles and energy resolution of prototype CZT strip detector

Position-sensitive strip CZT X-Ray detectors for use in X-Ray Astronomy have been developed by UCSD and WU which have very good energy resolution (e.g. 4.2 keV at 60 keV and 6.4 keV at 122 keV). (See Fig. 1) With lower noise electronics, such as described in Matteson et al.<sup>7</sup>, even better resolution can be obtained.

In order to obtain a better understanding of the performance of the detector, a modelling program was developed. The objective is to predict the spectra and the signal waveforms of X-rays interacting in a CZT strip detector. This requires determining the positions of interactions, propagating the electron-hole pairs, calculating the charges induced on electrodes and modelling pulse shaping electronics. At this time, the model does not account for X-ray interactions and electronic effects, but its calculations of charge transport and signal production are in very good agreement with the experimental measurements.

## 2. BASIC PRINCIPLES FOR THE MODEL

### 2.1. X-Ray Interactions

For the energy range of interest,  $\sim$  five - several hundred keV, interactions of photons with the detector are mostly photoelectric. For example at 100 keV photoelectric cross section is  $\sim$  10 times greater than the Compton scattering cross section. At 250 keV, the cross sections are equal.

Cd and Te have K edges at  $\sim$  25 keV and  $\sim$  31 keV respectively. So an X-ray with energy greater than 25 keV can produce a photoelectron and a characteristic K X-ray. Normally, the K X-ray will be absorbed within  $\sim$  100  $\mu$ m of the interaction position, unless the interaction is close to the physical boundaries of the detector, and it escapes. The photoelectron loses energy by creating electron-hole pairs. It will be stopped completely within a short distance, e.g., 30  $\mu$ m for 100 keV X-rays. This, along with thermal diffusion, causes an initial spreading of the electron-hole plasma.

### 2.2. Charge Transport

When bias is applied between anodes and cathodes, charges drift along the electric field lines. Up to fields of  $\sim$  10 kV/cm the drift velocity of electrons and holes are proportional to the field.<sup>8</sup> ( $v = \mu E$ , where  $\mu$  is the mobility.) For higher fields, they drift with a constant speed. In CZT, electrons move much faster than holes and typical mobilities are  $\mu_e \sim 1000 \text{ cm}^2 \text{ V}^{-1} \text{ s}^{-1}$ ,  $\mu_h \sim 50 \text{ cm}^2 \text{ V}^{-1} \text{ s}^{-1}$ , respectively.<sup>9,10</sup> A lower value of hole mobility,  $\mu_h \sim 15 \text{ cm}^2 \text{ V}^{-1} \text{ s}^{-1}$ , is also reported.<sup>11</sup>

### 2.3. Trapping and Detrapping

The charges can be trapped on their paths due to trapping sites in the crystal structure. The trapping can be quantified by trapping time  $\tau$  defined as mean free drift time of carriers before trapping occurs.<sup>12</sup> Both electrons and holes detrapp as well, which restores detector's charge neutrality. A useful quantity is the trapping length defined as:  $L(x) = (\mu \tau) E(x)$ . If the electric field is constant, the charge remaining as a function of distance is written as:

$$Q_{e,h}(x) = Q_{e,h}(0) \exp[-d/L_{e,h}(x)]. \quad (1)$$

where  $Q(0)$  is the total number of electron-hole pairs created and  $d$  is the distance from the interaction site. Since holes move much slower than electrons, they are more susceptible to trapping. The typical values found in the literature for electron and hole  $\mu\tau$  products are  $\mu_e\tau_e \sim 3 \times 10^{-3} \text{ cm}^2/\text{V}$ ,  $\mu_h\tau_h \sim 1 \times 10^{-4}$  to  $8 \times 10^{-6} \text{ cm}^2/\text{V}$ .<sup>10,13</sup> Those values correspond to a  $\tau_e$  of around  $3 \mu\text{s}$  and a  $\tau_h$  of  $2 \mu\text{s}$  to  $160 \text{ ns}$  respectively. For a typical field of  $1000 \text{ V/cm}$ , the corresponding trapping lengths are  $L_e \sim 3 \text{ cm}$  and  $L_h \sim 1 \text{ mm}$  to  $0.08 \text{ mm}$  respectively.

Detrapping is a complicated phenomenon whose effects depend on temperature, material and pulse shaping electronics. Its details are discussed by Martini et al.<sup>14</sup> and by Mayer.<sup>15</sup>

### 2.4. Charge Induction

The charge induced on each electrode can be calculated by the weighting potential method,<sup>16</sup>  $Q_{ind} = -Q(x) W(x)$ , where  $W(x)$ , the weighting potential, is a number between 0 and 1, and can be obtained by solving the Laplace equation in the system where unit potential is assigned to the particular electrode and the remaining electrodes are assumed to be grounded. Electron-hole pairs separate under the applied field, and, as they drift, they induce charges on each electrode with the relation above. Because of trapping, some charges do not reach the electrodes, and the total induced charge on an electrode is a function of an interaction's position. For a planar detector, an analytic solution to total charge induction as a function of depth is given by the Hecht equation<sup>17</sup>:

$$Q_{ind}/Q(0) = (L_e/D)(1 - \exp[-(D-x)/L_e]) + (L_h/D)(1 - \exp[-x/L_h]) \quad (2)$$

where  $D$  is the detector thickness and the interaction occurs at a distance  $x$  from the cathode. Note that the Hecht equation is valid only when detrapping within the integration time is negligible. For a strip detector the induced charge can be found numerically as in this paper, or can be calculated analytically by integrating the current equation.<sup>5,18</sup>

For a strip or pixel detector, an anode has strong weighting potential only in its vicinity due to its small size compared to the detector size. See Fig. 7 for an example. If illumination is from the cathode side, the holes trapped near the cathodes do not affect the anode signal since there is no appreciable weighting potential. Indeed, for the energy range in interest, most of the interactions are near the cathodes. Since electrons show good transport properties, they are collected at anodes. This is "the small pixel effect". Due to this effect, strip or pixel detectors yield superior performance to planar detectors.<sup>5,6</sup>

## 3. MODELLING

By using the principles explained above, a computer simulation of a CZT detector was developed that predicts induced charge on each electrode for various geometries. It consists of two parts: (1) calculation of electric fields and weighting potentials, and (2) charge drift, trapping and calculations of induced charge using the fields and potentials. The former is done with a commercial program, MAXWELL,<sup>19</sup> which, for a given geometry calculates the potentials and fields and saves the values to a file. Then a C program reads those values, and drifts charges on a rectangular grid. The grid is coarse at the cathode side ( $10 \mu\text{m}$ ) and fine ( $1 \mu\text{m}$ ) near the anode side to accurately follow the trajectory. Cathodes are at the top and the electrons move down on grid points following the electric field lines. If the grid size is  $M$ , depth on the grid is  $z$  and the interaction depth is  $z_o$ , then for electrons:

- $\Delta z = M$
- $\Delta t = M/(\mu_e E_z)$

- $\Delta x = \mu_e \dot{E}_x \Delta t$
- $L_e = \mu_e \tau_e (E_x^2 + E_z^2)^{1/2}$
- $Q(z) = Q(z-1) \exp(-(x^2 + M^2)^{1/2}/L_e)$  and  $Q_T(z-1) = Q(z) - Q(z-1)$
- $Q_{ind} = Q(z) W(z) + \sum_{i=z_0}^{z-1} Q_T(i) W(i)$

where  $Q_{ind}$  is the induced charge on a specific electrode and  $Q_T(i)$  is trapped charge at site  $i$ . A similar set of equations applies to holes. Induced charge is calculated for each electrode type.

A cautionary remark is needed here since for some geometries involving steering electrodes,  $E_z$  might change sign close to steering electrodes. Those cases must be treated carefully. (For example, for an interaction in this region, the holes prefer to drift to steering electrodes, instead of cathodes.)

The model assumes a linear field-velocity relation throughout the detector. The charges trapped are not de-trapped. Point charges are used, and there is no diffusion or initial spreading of electron hole plasma. The model does not include Compton scattering and K X-rays.

#### 4. EXPERIMENTAL SET UP

The detector modelled is a laboratory prototype which was developed to study techniques for X-ray imaging instruments such as HEXIS<sup>7</sup> and MARGIE.<sup>20</sup> There are 22 anode and 22 cathode orthogonal strips on the  $12 \times 12 \times 2$  mm<sup>3</sup> detector. (See Fig. 2.) In addition, there are steering electrodes in between anodes to enhance the charge collection. Steering electrodes are connected to each other. Anodes and steering electrodes are 100  $\mu$ m wide, cathodes are 450  $\mu$ m wide, and all have 500  $\mu$ m pitch. The anodes are biased at 200 V and steering electrodes at 180 V, so charges created above steering electrodes are directed to anodes. (See Fig. 3) A ceramic carrier holds the detector. The electrodes are coupled to Amptek A250 charge sensitive preamplifiers. Signals then are processed by shaping, amplifying and triggering circuits, and digitized by ADC's which give the total signal. An on-line program processes the data and builds multiple spectra according to various event selection criteria.<sup>7,21</sup> Off-line processing is also used.

The system also carries a planar detector with the same size as the strip detector, monitored by the same electronics. This gives an opportunity to compare the performance of strip detector to the planar detector.

An additional setup was used to measure pulse shapes from various electrodes. The detector was illuminated by X-ray sources with two Amptek A250 preamplifiers connected. Signals were recorded using a Tektronix DSA 601 four channel digital oscilloscope. The archive of those measurements includes various combinations of anodes, cathodes

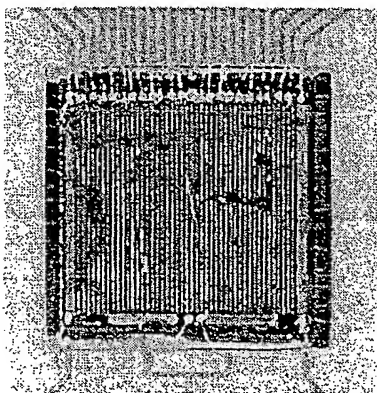


Figure 2. Prototype CZT strip detector. 22 anode strips with 500 microns pitch and 22 steering electrodes. Total size is  $12 \times 12 \times 2$  mm<sup>3</sup>.

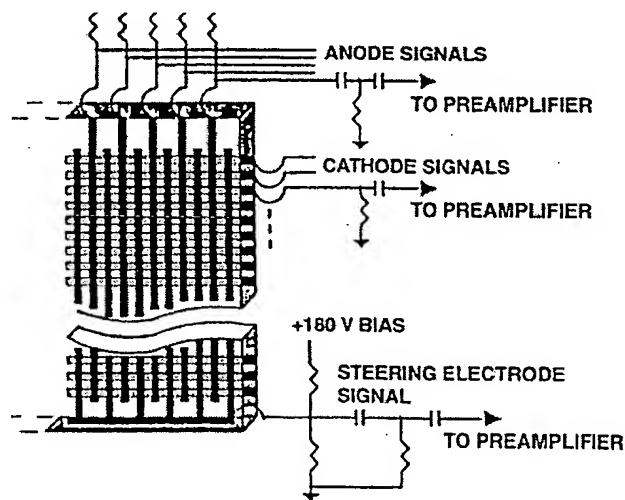


Figure 3. Detector electrode and bias network connections.

and steering electrodes. Sources used were  $^{57}\text{Co}$  which primarily emits 122 keV  $\gamma$ -rays which are fully absorbed, and  $^{137}\text{Cs}$  which emits  $\gamma$ -rays at 662 keV. These can Compton scatter and leave energies up to 382 keV in the detector.

To obtain transport properties, a set of measurements was made with an alpha particle source on a planar detector. The alpha beam was collimated to make it monoenergetic. The anode was coupled to an Amptek A250 preamplifier and the detector was illuminated from cathode side to determine electron transport properties. Then the bias was reversed to get hole transport properties. For bias voltages from 15 V to 210 V, the signals were recorded with the digital oscilloscope and the spectra were recorded by a ND76 Spectrum Analyzer.

## 5. RESULTS

### 5.1. TRANSPORT PROPERTIES

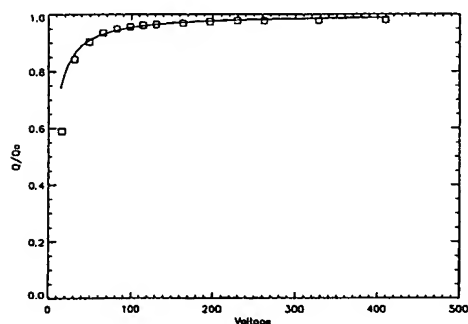


Figure 4. Measured peak height as a function of applied bias for alpha particles impinging on the cathode. Solid line is a fit to Hecht Equation, eqn(2).

The measurements done using the planar detector gave important insights. Spectra obtained from the motion of electrons had good energy resolution ( $\sim 3\%$  FWHM) for the electric fields greater than 1000 V/cm. The amplitudes were used to fit the Hecht equation (See Fig. 4), and a  $(\mu\tau)_e$  of  $5.5 \times 10^{-6} \text{ cm s V}^{-1}$  was obtained. For the holes however, 3  $\mu\text{s}$  shaping time of the amplifier caused a severe ballistic deficit effect. The peaks were very broad,  $\sim 80\%$  at any bias. This may be due to non-uniform hole trapping and electric field.<sup>8</sup>

The individual signal versus time curves were also used to obtain transport parameters. The mobility of electrons was measured by using the slope of the linear part of signal vs time.<sup>14,15</sup> See Fig. 5 for an example. The values were between 900 and 1100  $\text{cm}^2 \text{ V}^{-1} \text{ s}^{-1}$  with a mean of 960  $\text{cm}^2 \text{ V}^{-1} \text{ s}^{-1}$ . But even for high biases, signal versus time curves were not completely linear, and showed a gradual non-linear increase to the maximum. This is a typical sign of detrapping<sup>14,15</sup> which makes the Hecht equation fit questionable. Still, it gives an effective  $\mu\tau$ , and determined value obtained,  $5.5 \times 10^{-6} \text{ cm s V}^{-1}$ , is close to  $6.2 \times 10^{-6} \text{ cm s V}^{-1}$  which resulted in the best agreement with the measurements. (Fig. 13, Sect. 5.3.)

The slope method was also applied for the holes, and an average of  $\mu_h \sim 22 \text{ cm}^2 \text{ V}^{-1} \text{ s}^{-1}$  was obtained, which is smaller than usually found in the literature. Perhaps, an effective mobility was found with this method, since hole transit time (time required for carriers to transverse the detector) may be comparable to trapping and detrapping times.<sup>15</sup>

### 5.2. TRAJECTORIES AND WEIGHTING POTENTIALS

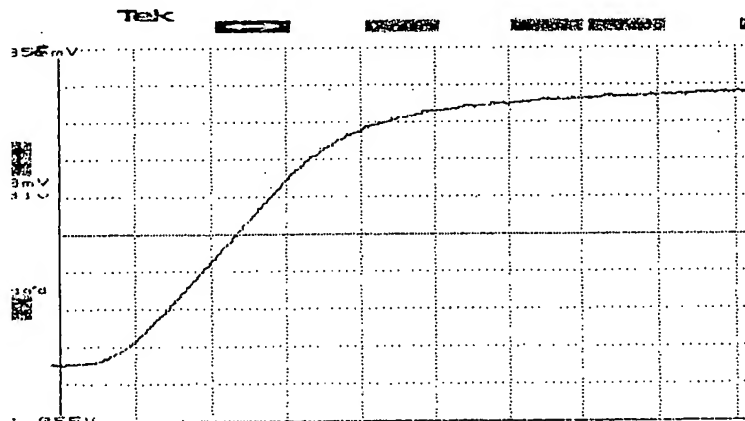


Figure 5. Signal versus time of an electrode when an alpha particle impinges on the cathode for a planar detector. The x-axis unit is 100 ns per division, and y-axis unit is 20 mV per division.

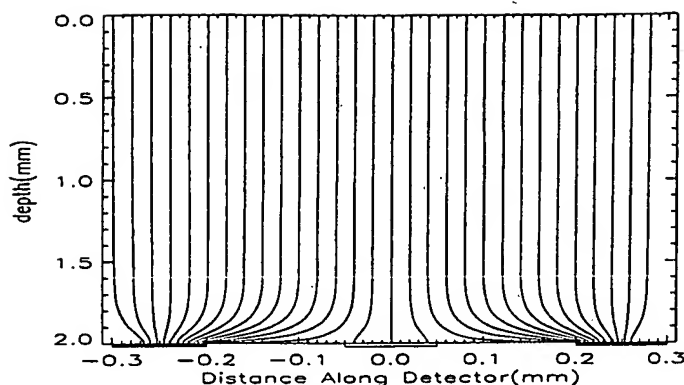


Figure 6. Model calculation of charge drift trajectories. (X- and y-axes are not scaled the same.) Filled boxes are anodes and empty boxes are steering electrodes here and in Fig. 7

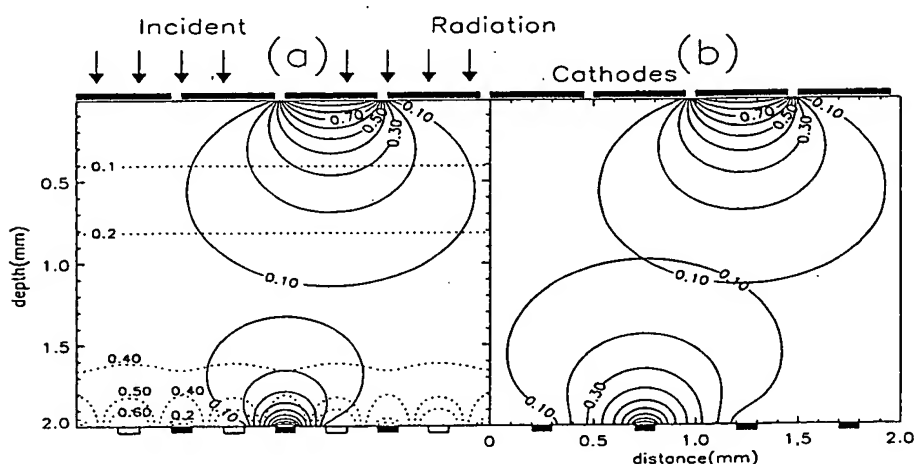


Figure 7. (a) Model calculation of weighting potential of the prototype detector. The dashed lines are steering electrodes weighting potential. (b) Model calculation of weighting potential without the steering electrode

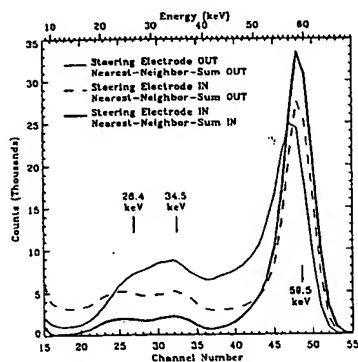


Figure 8. Effects of the steering electrode and nearest neighbor sum for an anode spectrum. Source is  $^{241}\text{Am}$ . From Matteson et al.<sup>2</sup>

Results of electric field calculations are shown in Fig. 6. It is clearly seen that most of the trajectories are directed onto the anodes by the steering electrode. However, some go to the steering electrodes and the gaps. For interactions at random positions near to the cathodes, 85% go to the anodes, 10% to the steering electrode, and 5% to the gap.

Figure 7a shows weighting potential distributions of all three types of electrodes. The cathode weighting potential extends deep into the detector, e.g.,  $W \sim 0.1$  at a depth of 1.2 mm. Steering electrode weighting potential is also very extended,  $W \sim 0.1$  at depth 0.4 mm. As discussed before, if weighting potential of an electrode is extended, signals from that electrode are affected by hole trapping. On the other hand, the weighting potential of the anodes is localized to the immediate vicinity of the anodes. Thus, the anodes benefit from the small pixel effect.

It was well established that addition of steering electrodes to the detector improved energy resolution.<sup>2</sup> Figure 7b explains the main reason for this. Without the steering electrodes, weighting potential of the anode extends fur-



ther, reducing the small pixel effect. The effect of relative biasing is also modelled. When there is no bias between steering electrodes and anodes, 20% of the trajectories end up in the gap, which would result in incomplete charge collection. Also from the remaining 80%, half of them end up in steering electrode which does not provide position information. Fig. 8 shows the difference in spectra when there is biasing and there is no biasing.

### 5.3. DEPTH OF INTERACTION

Weighting potential curves clearly indicate that the amplitude of the signals is a function of depth of interaction. This effect, which causes a low energy tail due to incomplete charge collection, was studied with the model by calculating the total signals for interactions at various depths. An electron trapping length of 6 cm and hole trapping length of 0.24 mm were used. Fig. 9 shows the results. For the anodes, the response is uniform to  $\pm 2\%$  for depths less than 1.7 mm. For the depth greater than 1.8 mm, the anode signal amplitude becomes lateral position dependent. Typically, useful signals are produced on several neighboring cathode strips due to trapping of holes. Fig. 10 is an example of this which shows signals of two neighboring cathodes as a function of time. For the single cathode with the largest signal, Fig. 9 shows a rapid decrease in signal with depth. When the two neighboring cathode signals are added, the depth dependence is much less severe. Therefore by adding neighboring cathode signals to the one which has the maximum signal, better spectra can be obtained (See Fig.11).

The model was tested with a series of experiments. Data were collected by flood illumination with  $^{57}\text{Co}$  at 122 keV. For each event, the ratio of cathode to anode signal and steering electrode signal were determined. These were plotted as a scatter plot in Figure 12 along with the model predictions. The agreement is very good. This technique was used by Slavits et al.<sup>21</sup> to reduce background by rejecting events which were not incident X-rays.

It has been mentioned before that cathode to anode ratio is a monotonic function of depth.<sup>2</sup> Relative anode signal versus cathode to anode ratio is plotted along with the model prediction. The agreement is very good, except at a very small region with high cathode to anode ratios. (See Figure 13.)

The model results were used to correct for the dependence of signal on depth of interaction and thus improve energy resolution. Pulse heights were multiplied by correction factors which were obtained from the model, using the cathode to anode ratio. Results are shown in Figure 14. In the corrected spectrum, interactions deeper than 1.7 mm have been discarded. This means discarding 18% of the events for 100 keV and less than 1% for 60 keV. There is significant improvement in energy resolution. The corrected spectrum has energy resolution of 7 keV whereas the uncorrected neighbor summed spectrum has 10.5 keV energy resolution at 122 keV. For comparison, a spectrum obtained from the top 0.05 mm of the detector is also plotted. This region presumably has the best energy resolution.<sup>22,2</sup> There is almost no difference between two spectra. The low energy tail is eliminated and the shape is symmetric. This method can be implemented in the software very easily.

### 5.4. SIGNAL VERSUS TIME

Depending on the interaction position, there are various types of signal behavior of the electrodes. Several examples are shown in the following, which are modelled with following parameters:  $\tau_e = 6 \mu\text{s}$ ,  $\mu_e = 1000 \text{ cm}^2 \text{ V}^{-1} \text{ s}^{-1}$  and  $\tau_h = 645 \text{ ns}$  and  $\mu_h = 40 \text{ cm}^2 \text{ V}^{-1} \text{ s}^{-1}$ . Fig.15 shows the general results for a typical interaction at  $200 \mu\text{m}$ . The anode signal rises slowly until electrons reach significant weighting potential (See Fig. 7a). Then, it rises rapidly with a typical risetime of 50-70 ns. Only 3% of the electrons are trapped. On the other hand, the cathode signal increases promptly due to its extended weighting potential. This signal usually consists of two parts, (1) a rapid component due to electrons drifting away from the cathode (they move to lower weighting potential) and (2) a slow component due to holes approaching the cathodes. Charge collection is incomplete due to trapping. Fig. 15e shows a typical signal with all the features described above, measured with our setup with  $^{57}\text{Co}$ .

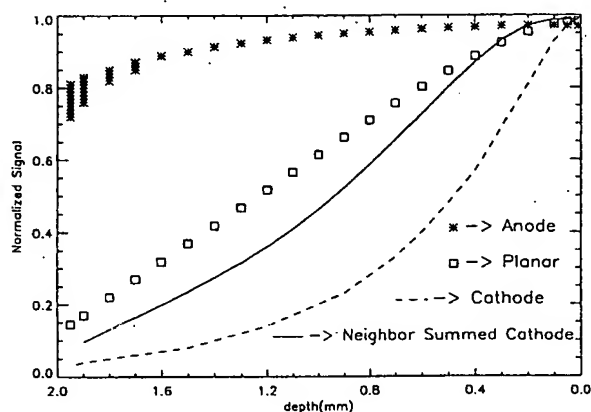


Figure 9. Model calculations of total signals at electrodes of prototype strip detector and planar detector.

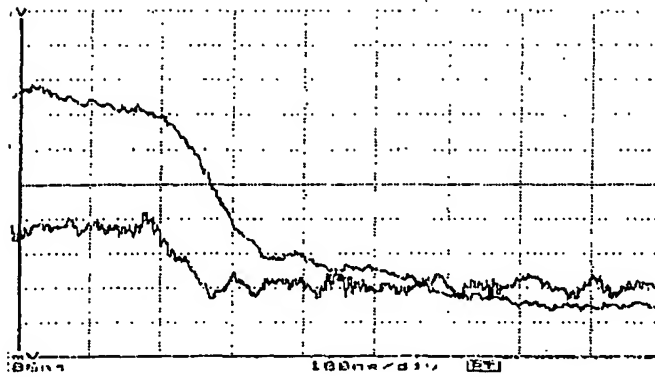


Figure 10. Typical cathode and neighboring cathode signals as a function of time. X-axis is 100 ns per division and y-axis is 1 mV per division.

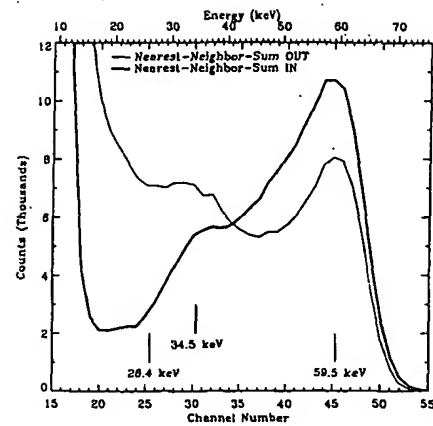


Figure 11. Effect of nearest neighbor sum for a cathode spectrum. Source is  $\text{Am}^{241}$ . From Matteson et al.<sup>2</sup>

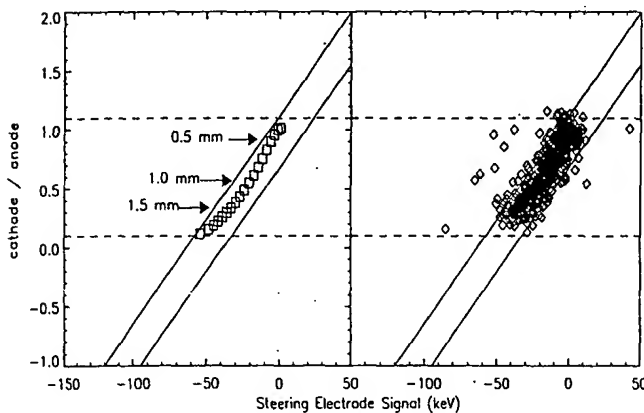


Figure 12. Modelled (left) and measured (right) depth of interaction effect on cathode to anode ratio and steering electrode signal for 122 keV X-rays.

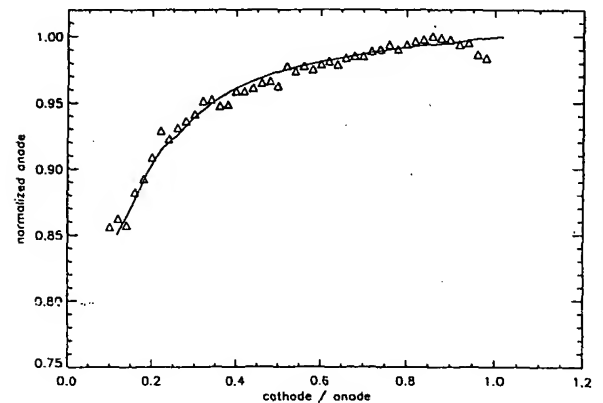
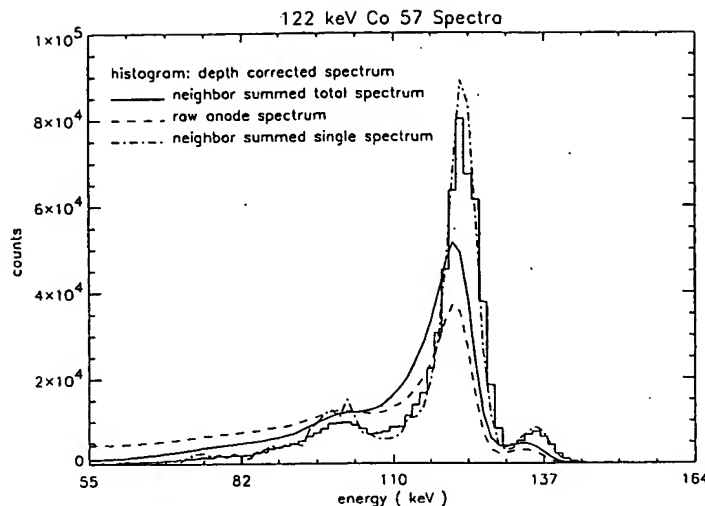


Figure 13. Anode signal versus cathode to anode ratio. Triangles are measurements for 122 keV and solid line is the model prediction.

A second example (Figure 16) illustrates the behavior of signals on the steering electrode when electrons are collected at an anode. The interaction is at  $600\ \mu\text{m}$ . The signal first rises rapidly but then drops to a negative value. Then it rises very slowly. To understand this, recall Fig. 7a. The weighting potential of the steering electrodes rises, down to a depth of 1.6 mm, then drops quickly to zero near the anodes. The modelled signal drops down not to zero but negative values because of trapped holes. The slow increase at the end is due to untrapped holes going away from the steering electrodes. The measurements (See Fig. 16e for a typical signal) show those properties. For the case of an event at the very top, like the first example, steering electrode signal drops to zero (Figure 15b) since most of the holes are not trapped and weighting potential is very low. One discrepancy between simulations and measurements is the fall time of the steering electrode signal after electrons are collected by anodes. Fall times of  $\sim 50\ \text{ns}$  are predicted, but instead,  $\sim 150\ \text{ns}$  are observed.

Results of electric field calculations show that for some of the interactions, the electrons can drift to the steering



**Figure 14.** Comparison of depth corrected spectrum (histogram) with uncorrected spectra. Neighbor summed single spectrum is obtained from the top 0.05 mm of the detector. See Section 5.3 for details.

electrodes, or even to the gaps between steering electrodes and anodes. These two cases were modelled also. Fig. 17 shows the case where electrons end up at a steering electrode for an interaction at 0.2 mm. The rise time on the steering electrode signal is greater than that on the anode. The anode signal in this case, rises first and goes down to almost zero since weighting potential is very low at the depths where trapped holes are located. Fig. 17e shows a measured steering electrode signal for  $\text{Cs}^{137}$  which agrees with the model.

What happens when electrons reach the gaps is unknown. It is modelled with idealized surface conditions for which an electron stops when it reaches the surface. The surface of a semiconductor crystal has a lot of imperfections and therefore has a lot of trap centers for the free charges. Basically, the model treats electrons as trapped when they reach the surface. Fig. 18 shows an example. Both anode and steering electrode do not collect full charge. The steering electrode signal (Fig. 18b) first increases to the maximum as usual, then decrease some, since electrons are directed to the anodes. However, they can not reach the anode, therefore induce a positive signal at the steering electrode. (Compare with the case when electrons reach the anode, the steering electrode signal is negative in this case due to trapped holes.) One of the measurements for the steering electrode showed a similar behavior expected from such interaction (Figure 18e). The timescales and amplitude are consistent with the model. If this interpretation is true, then the electrons move slower very close to the surface and then trapped. The slow increase at greater timescales is due to holes moving away from the steering electrodes.

## 6. CONCLUSIONS AND FUTURE DIRECTIONS

The model is able to predict correctly the fundamentals of how our detector works. In terms of predicting total signals, it agrees within 1% with the measurements (See Fig. 13). This shows that some parameters that are not included in the program, such as diffusion, and range of photoelectron do not affect the performance of the detector very much. In terms of temporal behavior, the model is within 10% -20% when parameters that are usually found in literature are used. The discrepancies may be due to pulse shaping of electronics or detrapping which was observed for the planar detector. (See section 5.1.)

Trajectory and weighting potential calculations helped us to understand the improvement obtained with adding steering electrode to the system. It is also shown that, the small pixel effect is a result of not only the size of the electrode, but also the distance between electrodes (See Fig. 7). With this in mind, an optimized geometry for enhancing the small pixel effect was studied. In this geometry, anodes are  $50\text{ }\mu\text{m}$  wide and steering electrodes are  $250\text{ }\mu\text{m}$  wide. Pitch size is  $500\text{ }\mu\text{m}$ . More bias is applied between steering electrodes and anodes in order to decrease trajectories ending at wide steering electrodes. Preliminary model results showed an increase from 85% to > 90% in relative anode signal for very deep interactions compared to detector used now. A detector with this design will be tested later this year.

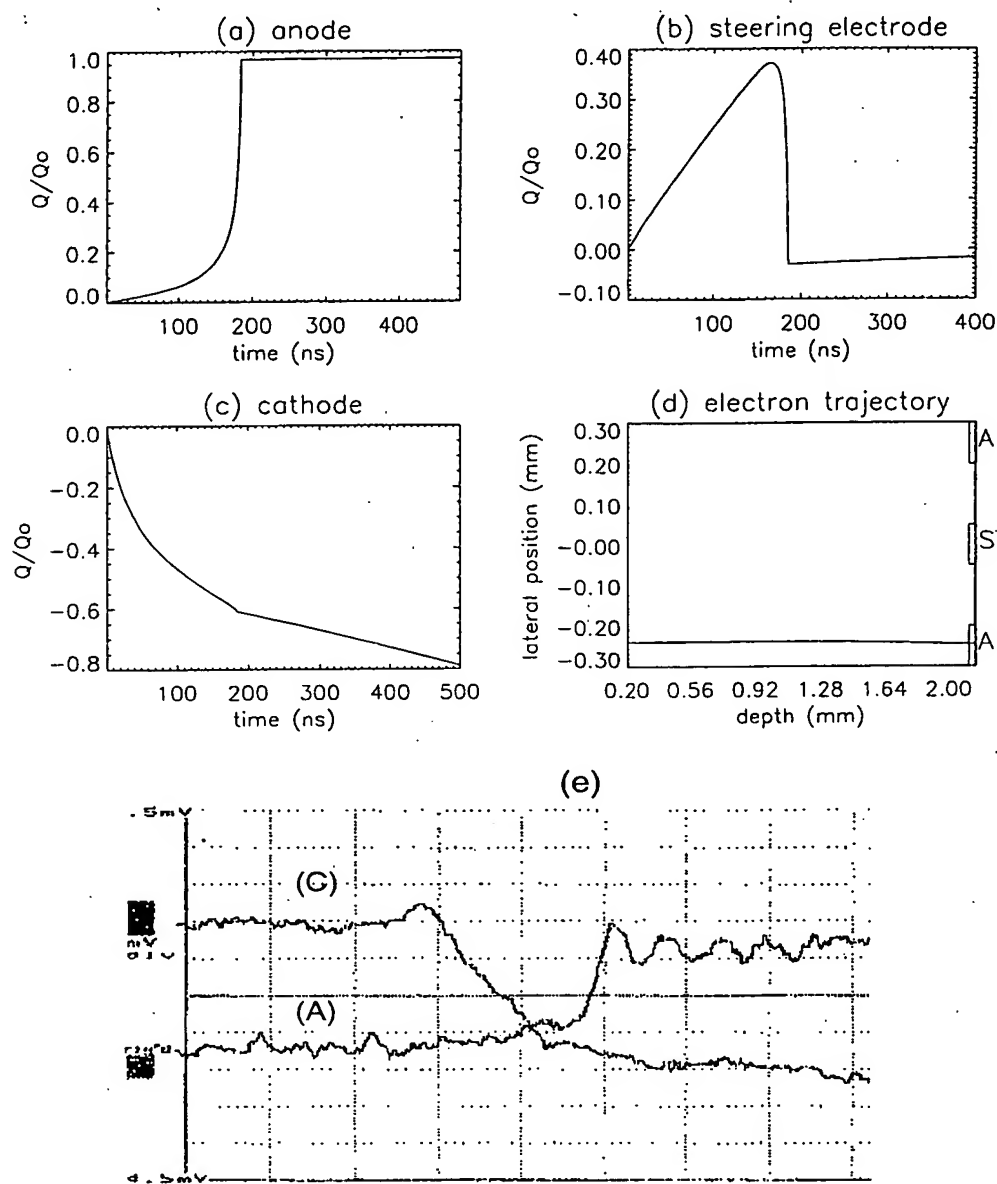
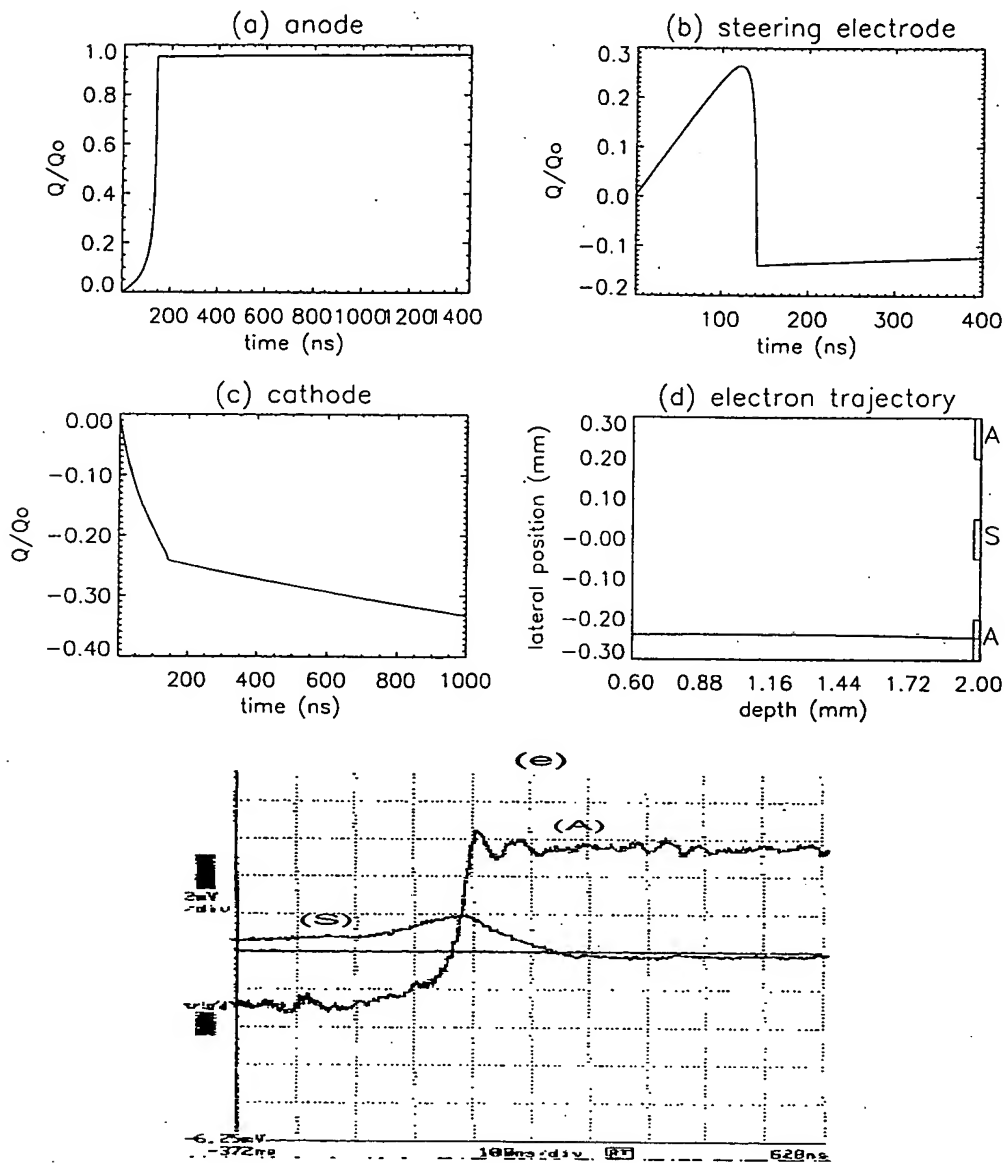


Figure 15. Modelled, (a)-(c), and measured waveforms, (e), and modelled trajectory, (d), for an interaction at  $200\text{ }\mu\text{m}$  depth. In (e), the cathode (C) gain is 1.67 times the anode (A) gain. The x-axis unit is 100 ns per division and y-axis unit is 1 mV per division. The overshoot and ringing of anode signal is due to preamplifier response to the short risetime of the signal. See Sect. 5.4 for details.

Both cathode and steering electrode signals are strongly depth dependent. Depth of interaction information, which can be obtained using the model, can be used to reject background<sup>21</sup> and to improve the energy resolution, as demonstrated in this paper.

The model will be improved by adding a Monte-Carlo code to simulate X-ray interactions in the detector. Detrapping and modelling of electronics will also be included. Signals obtained from each interaction will be used to build a spectrum, so that the model will be able to predict the energy resolution of detectors with different geometries and biasing schemes for the electrodes.

The predictions of trajectory calculations will be tested by localizing the X-ray interaction with a  $30\text{ }\mu\text{m}$  collimated beam which is positioned by a precision X-Y stage.<sup>4</sup> In particular, this will allow us to study the case when electrons



**Figure 16.** Modelled, (a)–(c), and measured waveforms, (e), and modelled trajectory, (d), for an interaction at 600  $\mu\text{m}$  depth. In Fig. (e), the steering electrode (S) gain is 1.67 times the anode (A) gain. The x-axis unit is 100 ns per division and y-axis unit is 2 mV per division. See Sect. 5.4 for details

reach the gap.

More experiments will be done on planar detector to understand the transport properties, especially detrapping. Homogeneity of the material will be studied by using the collimated beam.

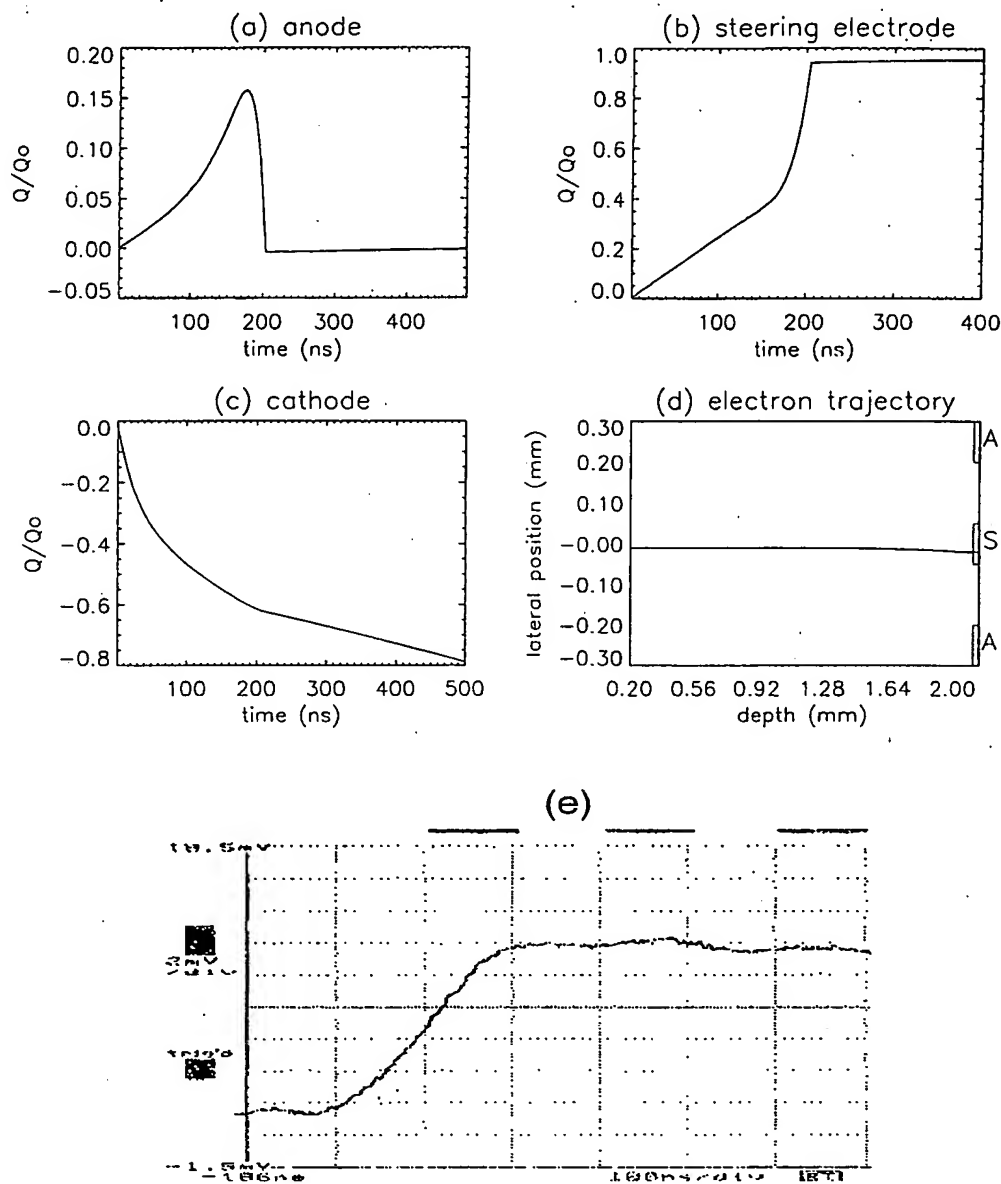


**Figure 17.** Modelled, (a)–(c), and measured, (e), waveforms and trajectory, (d), for an interaction in which electrons drift to steering electrodes. The depth is 200  $\mu\text{m}$ . In (e), the x-axis is unit 100 ns per division and y-axis unit is 2 mV per division. Events ending on the surface of steering electrodes constitute  $\sim 10\%$  of all interactions. See Sect. 5.4 for details.

#### ACKNOWLEDGMENTS

This work was supported by NASA SR&T Grant NAG5-5111 and at WU by NASA SR&T Grant NAG5-5114 and NASA GSRP Grant NGT-50170. Technical support was provided at UCSD by Fred Duttweiler, George Huszar, Charles James, Sandy O'Brien, Phillippe Leblanc, David Malmberg, Ron Quillan and Ed Stephan, and at Washington University by Paul Dowkontt, John Epstein, and Garry Simburger. We would also like to thank to Pat Lamers at Ansoft for providing MAXWELL. Emrah Kalemci was partially supported by TUBITAK.

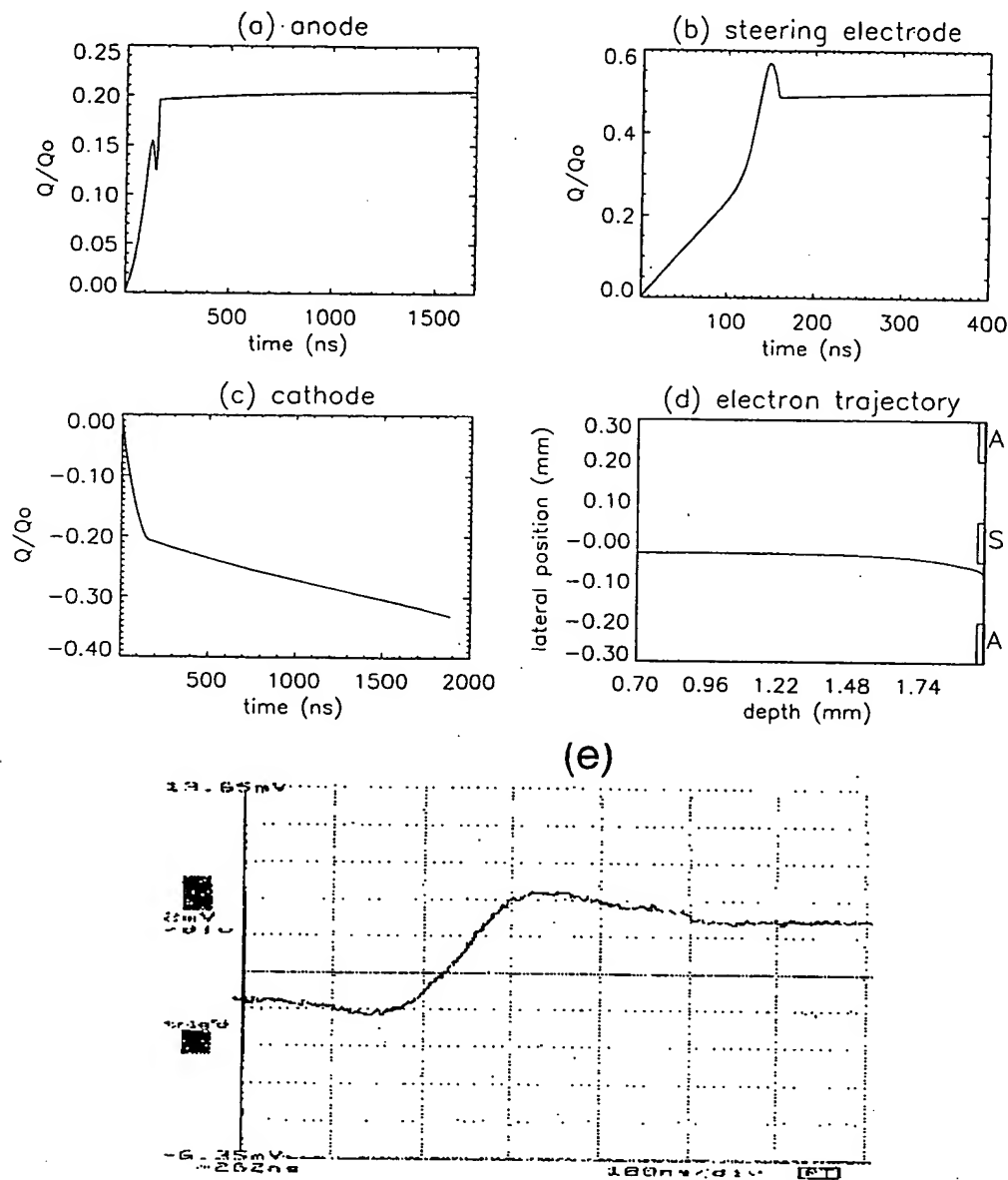


**Figure 18.** Modelled waveforms, (a)–(c), and trajectory, (d), for an interaction at a depth of 700  $\mu\text{m}$ . In this case, electrons never reach the anode, but collect in the gap. Fig. 17e is a measured waveform which appears to be a gap event. The x-axis unit is 100 ns per division and y-axis unit is 2 mV per division. See Sect. 5.4 for an extended discussion.

## REFERENCES

1. 15 Year Plan for X-ray Astronomy, 1994-2008, Report of the X-ray Astronomy Program Working Group, NP-213, NASA Headquarters, High Energy Astrophysics Branch, 1994.
2. J. L. Matteson, F. Duttweiler, G. L. Huszar, P. C. Leblanc, R. T. Skelton, E. A. Stephan, P. L. Hink, P. W. Dowkontt, K. R. Slavis, T. O. Tumer, and S. D. Kravis, "Position-sensitive CZT detector module," in *Hard X-Ray and Gamma-Ray Detector Physics and Applications*, F. P. Doty, ed., *Proc. SPIE* 3446, pp. 192-203, 1998.

3. J. L. Matteson, W. Coburn, F. Duttweiler, W. A. Heindl, G. L. Huszar, P. C. Leblanc, M. R. Pelling, L. E. Peterson, R. E. Rothschild, R. T. Skelton, P. L. Hink, and C. Crabtree, "CdZnTe arrays for astrophysics applications," in *Hard X-Ray and Gamma-Ray Detector Physics and Applications*, R. B. Hoover and F. P. Doty, eds., *Proc. SPIE* 3115, pp. 160-175, 1997.
4. J. L. Matteson, W. Coburn, F. Duttweiler, T. Gasaway, W. A. Heindl, P. C. Leblanc, D. R. MacDonald, M. R. Pelling, L. E. Peterson, R. E. Rothschild, R. T. Skelton, P. Hink, and C. Crabtree, "CdZnTe strip detectors for high-energy x-ray astronomy," in *Hard X-Ray / Gamma-Ray and Neutron Optics, Sensors, and Applications*, R. B. Hoover and F. P. Doty, eds., *Proc. SPIE* 2859, pp. 58-73, 1996.
5. H. H. Barret, J. D. Eskin, and H. B. Barber, "Charge transport in arrays of semiconductor gamma-ray detectors," *Phys. Rev. Lett.* 75,1, pp. 156-159, 1995.
6. P. N. Luke, "Electrode configuration and energy resolution in gamma-ray detectors," in *Proceedings of the 9th International Workshop on Room Temperature Semiconductor X- and Gamma-Ray Detectors, Associated Electronics and Applications, Grenoble, France*, 1995.
7. J. L. Matteson, D. E. Gruber, W. A. Heindl, M. R. Pelling, L. E. Peterson, R. E. Rothschild, R. T. Skelton, P. Hink, K. R. Slavis, and W. R. Binns, "High energy x-ray imaging spectrometer - HEXIS," in *EUV, X-Ray, and Gamma-Ray Instrumentation for Astronomy IX*, *Proc. SPIE* 3445, pp. 445-457, 1998.
8. P. Doty, Personal Communication.
9. Z. He, G. F. Knoll, D. K. Wehe, and Y. F. Du, "Direct measurement of electron drift parameters using depth-sensing single-carrier CdZnTe detectors," in *Semiconductors for Room-Temperature Radiation Detector Applications II*, *Mat. Res. Soc. Symp. Proc.* 487, pp. 89-94, 1997.
10. Y. Eisen and A. Shor, "CdTe and CdZnTe room-temperature x-ray and gamma-ray detectors and imaging systems," in *Semiconductors for Room-Temperature Radiation Detector Applications II*, *Mat. Res. Soc. Symp. Proc.* 487, pp. 129-146, 1997.
11. O. Tousignant, L. A. Hamel, J. F. Courville, J. Macri, M. Mayer, M. L. McConnell, and J. M. Ryan, "Transport properties and performance of CdZnTe strip detectors," *IEEE Trans. on Nucl. Sci.* 45, 3, pp. 556-560, 1998.
12. G. F. Knoll, *Radiation Detection and Measurement*, John Wiley & Sons, New York, 1979.
13. P. N. Luke and E. E. Eissler, "Performance of CdZnTe coplanar-grid gamma ray detectors," *IEEE Trans. on Nucl. Sci.* 43, 3, p. 1481, 1996.
14. M. Martini and T. A. McMath, "Trapping and detrapping effects in lithium-drifted germanium and silicon detectors," *Nucl. Instr. and Meth.* 79, pp. 259-276, 1979.
15. J. W. Mayer, "Semiconductor materials for gamma-ray spectroscopy," in *Semiconductor Detectors*, G. Bertolini and A. Coche, eds., pp. 445-496, John Wiley & Sons, New York, 1968.
16. S. Ramo, "Currents induced by electron motion," *Proc. I.R.E.* 27, pp. 584-585, 1939.
17. K. Hecht, "Zum mechanismus des lichtelektrischen primarstromes in isolierenden," *Z. Physik* 77, p. 235, 1932.
18. L. A. Hamel, J. R. Macri, C. Stahle, J. Odom, F. Birsa, P. Shu, and F. Doty, "Signal generation in CdZnTe strip detectors," *IEEE Trans. on Nucl. Sci.* 43, 3, pp. 1422-1426, 1996.
19. MAXWELL, *A Software to Solve Electromagnetic Problems*, ANSOFT, Four Station Square, Suite 660, Pittsburgh, PA 15219 USA.
20. M. L. Cherry, D. L. Band, J. Buckley, T. G. Guzik, P. Hink, J. R. Macri, J. L. Matteson, M. L. McConnell, T. J. O'Neill, J. M. Ryan, J. G. Stacy, and A. D. Zych, "MARGIE: An ultra-long duration balloon instrument for wide-field-of-view high-angular-resolution hard x-ray astronomy," in *EUV, X-Ray, and Gamma-Ray Instrumentation for Astronomy X*, *Proc. SPIE*, 1999.
21. K. Slavis, P. Dowkontt, F. Duttweiler, J. Epstein, P. L. Hink, G. L. Huszar, P. Leblanc, J. L. Matteson, R. T. Skelton, and E. Stephan, "High altitude balloon flight of CdZnTe detectors for high energy x-ray astronomy," in *EUV, X-Ray, and Gamma-Ray Instrumentation for Astronomy IX*, *Proc. SPIE* 3445, pp. 169-184, 1998.
22. Z. He, G. F. Knoll, D. K. Wehe, and J. Miyamoto, "Position-sensitive single carrier CdZnTe detectors," *NIM A* 388, pp. 180 - 185, 97.



# Depth Measurement in a Germanium Strip Detector

E. A. Wulf, J. Ampe, W. N. Johnson, R. A. Kroeger, J. D. Kurfess, and B. F. Philips

**Abstract**—We have demonstrated the ability to determine the depth of a gamma-ray interaction point over the full active volume of a thick germanium strip detector. This capability provides depth resolution of less than 0.5-mm full width half maximum (FWHM) at 122 keV in a device 11 mm thick with a 2-mm strip pitch. Fifty channels of electronics have been developed and tested with a 25 × 25 germanium orthogonal strip detectors. Experiments examining the capabilities of the system and demonstrating a simple Compton telescope using a single detector have been performed.

**Index Terms**—Gamma-ray imaging, position measurement, radiation detectors, semiconductor devices, spectroscopy, time measurement.

## I. INTRODUCTION

GERMANIUM strip detectors combine excellent energy resolution for gamma-ray detection with good two-dimensional (2-D) resolution. With the addition of depth information these detectors have excellent overall position resolution. Orthogonal strips on the front and rear faces of the crystal allow germanium strip detectors to locate a gamma-ray interaction in two dimensions accurate to the width of the strips. A gamma-ray interacts in the crystal and its position is determined by the intersection of the triggered strips on opposite sides of the detector [1]. The depth of the interaction is determined by looking at the timing difference between signals from collection of holes on one side of the detector and electrons on the other side as was recently demonstrated by [2] and [3]. The excellent energy resolution of germanium detectors makes it possible to determine if the signals collected at the front and back are from the same gamma-ray interaction. A germanium detector with submillimeter resolution in three dimensions is of interest in gamma-ray astrophysics for the next generation of instruments. It should also have the potential to improve the resolution of positron emission tomography (PET) [4]. Another application is for the GRETA detector under study for use in nuclear physics experiments by the Department of Energy [5].

The detector used for this work and the work of [2] is a 25 × 25 germanium orthogonal strip detector with 0.2-cm strip pitch that is 5 × 5 × 1.1 cm deep [1]. It has lithium strips held at +1.5-kV bias potential that collect electrons and boron strips on the opposite face to collect the holes.

Manuscript received November 21, 2001; revised April 15, 2002. This work was supported in part by the National Aeronautics and Space Administration (NASA).

E. A. Wulf, W. N. Johnson, R. A. Kroeger, J. D. Kurfess, and B. F. Philips are with the Naval Research Laboratory, Washington, DC 20375 USA (e-mail: wulf@gamma.nrl.navy.mil; johnson@gamma.nrl.navy.mil; kroeger@gamma.nrl.navy.mil; kurfess@gamma.nrl.navy.mil; philips@gamma.nrl.navy.mil).

J. Ampe is with Praxis, Inc., Alexandria, VA 22304 USA (e-mail: ampe@gamma.nrl.navy.mil).

Digital Object Identifier 10.1109/TNS.2002.801526

The interaction depth is directly related to the time difference between when the electron and hole signals are collected on opposite sides of the detector. This can be seen in Fig. 1, which shows that for an event occurring near the boron face of the detector it takes 113 ns for the electrons to travel to the lithium face. The simplest way to conceptualize measuring the time difference between charge collection is to determine the difference between the times when each of the preamplified signals crosses 50% of its total value. The timing difference in a 1.1-cm-thick detector is approximately ±120 ns for conversion near the front or the back of the detector.

## II. ELECTRONICS

To instrument a detector for depth information, one must determine the time difference between charge collection as well as the energy of the interaction. To determine the energy of an interaction, shaping amplifiers and analog to digital converters (ADC) are needed for all 50 strips. The depth determination requires a discriminator on each of the strips on the front and back of the detector and a time to digital converter (TDC) or the equivalent to measure the relative timing of the signals.

A major design question is whether a constant fraction discriminator (CFD) is necessary or if a simple leading edge discriminator (LED) is adequate for the relative timing of the signal rise. One type of CFD works by making two copies of the input signal, inverting and delaying one copy, attenuating the amplitude of the other and adding the two signals. This creates a zero crossing that occurs when the original signal was a fixed percentage of its full value. This is useful for eliminating time walk as a function of amplitude. The problem with CFDs in this application is that 150 ns of delay are necessary. This may be difficult to implement in future compact, low-power electronics. In contrast, an LED triggers when the input signal goes over a specific voltage and therefore can trigger at different times for different pulse amplitudes. This may not be a large issue for the germanium strip detector because the amplitude of the signals on the front and back of the detector are the same and the time walk is expected to be similar.

To read out all 50 strips on the detector with both energy and depth information requires 50 channels of shaping amplifiers, 50 channels of discriminators, 50 channels of ADCs, and 50 TDC channels. A decision was made to create a Nuclear Instrument Module (NIM) module that incorporated the shaping and discriminator functions in order to reduce the total number of modules. The outputs from eV5093 preamplifiers are fed into a buffer amplifier with a gain of 20 (see Fig. 2). The signal is then split and one copy is shaped by a four-pole shaper with a fixed gain and is fed to an ADC. Another copy of the amplified preamplifier signal goes to a fast shaper with an integration and differentiation time of 50 ns. The output of the fast shaper is run

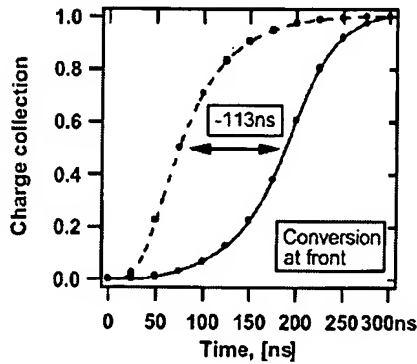


Fig. 1. The digitized preamplified signals from a germanium strip detector. The dashed curve is the signal as holes are collected on the boron side of the detector which is closest to the  $^{241}\text{Am}$  source. The solid curve is from the lithium side as the electrons are collected. There is a 113-ns difference in the time when the signals reach their midpoint [2].

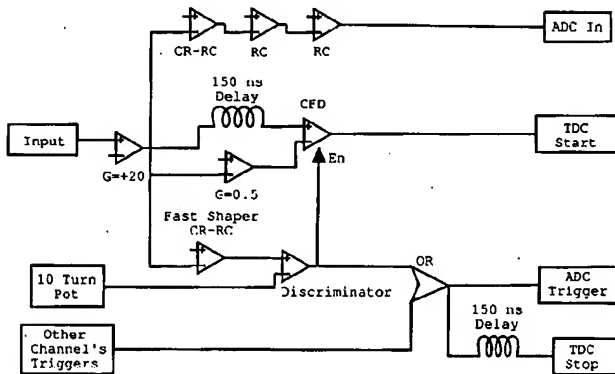


Fig. 2. A schematic of the NIM electronics constructed at NRL and used to instrument the  $25 \times 25$  germanium strip detector.

to a discriminator and compared to a dc level set by a front panel potentiometer. The output of the discriminator is summed with all other channels and used as a master trigger to start the ADC and as a common stop for the TDC. Another copy of the discriminator output is used to enable the comparator used in the CFD electronics.

The CFD section is composed of two copies of the amplified preamplifier signal. One copy is delayed by 150 ns and the other is attenuated to 50% of its original amplitude. These two signals are fed into a comparator that fires when the two signals have the same amplitude. In effect, this produces a signal when the preamplifier signal has risen to half of its total value. The CFD signal is used to start a TDC channel for each front and back strip.

Each electronics board supports four detector channels and four boards are included in one double wide NIM module (see Fig. 3). The outputs from these modules are fed into TDCs and ADCs residing in a CAMAC crate which is read out by a PC running Linux. The data is recorded on an event by event basis and saved to disk and tape for later analysis. This system maintains the excellent energy resolution, 1.6 keV at 122 keV, of a germanium detector as can be seen from a typical  $^{57}\text{Co}$  spectrum in Fig. 4.

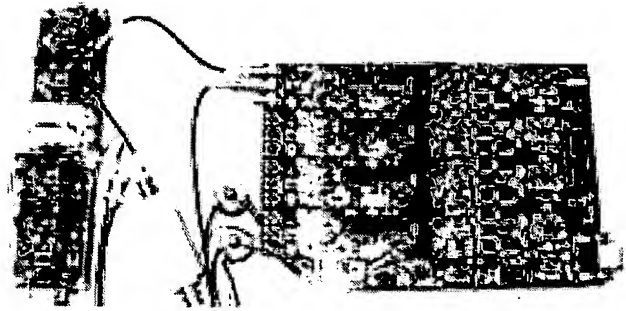


Fig. 3. A picture of one of the NRL electronics boards with four channels. Four of these boards are packaged together to produce one double-wide NIM module. The module to the left is a board holding multiple eV5093 preamplifiers that were used to produce test signals.

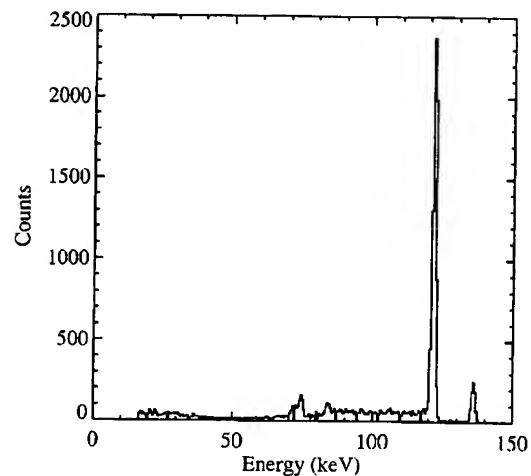


Fig. 4. Spectrum of  $^{57}\text{Co}$  source as measured with the germanium strip detector and the NIM electronics.

### III. DEPTH MEASUREMENTS

#### A. Detector Attenuation

The depth capabilities of the detector are demonstrated by observing the attenuation of gamma-rays as they pass through the detector. These tests confirmed that the depth of the interaction could be measured but are not an accurate way to determine the actual depth resolution of the system. The attenuation experiment was done by placing a source near the boron face of the detector and producing a histogram of the time difference in charge collection between the boron and lithium face. Each event histogrammed had to have only one strip with a signal on both the lithium and boron side and each signal had to be the correct energy to within 5 keV.

$^{57}\text{Co}$  has a 122 keV gamma-ray line that is attenuated 85% by the detector volume. The radiation length is 5.75 mm, which is approximately half the detector thickness. A plot of the number of counts as a function of time difference between charge collection on the front and back face is shown in Fig. 5. The face of the detector that was closest to the source was the boron face which corresponds to negative time differences and the lithium face to positive differences. The theoretical exponential attenuation of the germanium is shown superimposed as the dashed

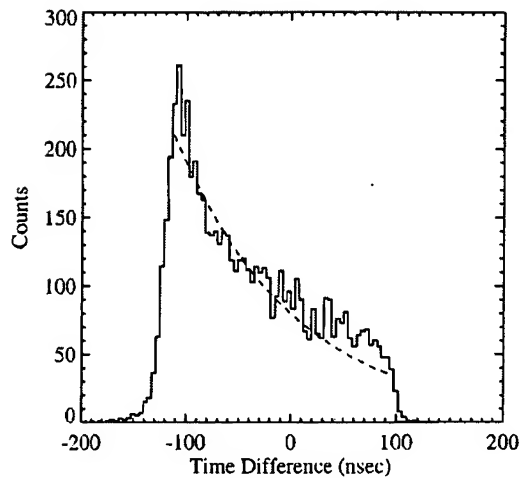


Fig. 5. The number of photo-peak events for the 122-keV gamma-ray line from  $^{57}\text{Co}$  as a function of time difference between charge collection on the boron and lithium face. The source was placed 40 cm from the boron face of the detector. The dashed line is the theoretical exponential attenuation of the gamma-rays by the germanium that makes up the detector.

line on the plot. The total time difference is shown to be 215 ns for the 1.1-cm-thick detector. This is similar to the total time difference found by [2]. The 15 ns difference between hole collection on the boron side and electron collection on the lithium side is due to the difference in drift velocities in germanium. At the detector's bias voltage of 1500 V and a temperature of 80 K, the drift velocity of the holes is  $7.5 \times 10^6$  cm/s, and that of the electrons is  $8.3 \times 10^6$  cm/s [6]. Using a detector thickness of 1.1 cm yields a total time difference that is larger than observed by 25%. This suggests a small nonlinearity in depth timing near the surfaces. The experiment was also performed with  $^{241}\text{Am}$  and  $^{137}\text{Cs}$ , which showed good agreement with the theoretical exponential attenuation curves. The differences between the attenuation curve and the measured values are most probably due to variations in the electric field near the surfaces of the detector, variations in the contaminants in the germanium, and not being able to sort out pure photoelectric events.

### B. Fan Source Scan

To test the depth resolution of the detector, the side of the detector was illuminated with a tightly collimated gamma-ray beam. A 1-mCi  $^{57}\text{Co}$  source was mounted in a collimator consisting of two flat planes of tantalum approximately 11.5 cm in length and 2 cm thick. The two planes are separated by 0.1-mm-thick spacers. This produces a well defined fan beam useful for scanning the detector. The fan source was scanned along the side of the detector using an  $x$ - $y$  position table. The table has a position resolution of 0.025 mm and a range of 10.2 cm. The source was moved in 0.5-mm steps and data was collected at each point along the side of the detector.

A histogram of the timing difference between charge collection on each boron strip and any lithium strip was constructed. For each event, only one lithium and one boron strip could have a signal and their energies had to be within 5 keV of the 122 keV

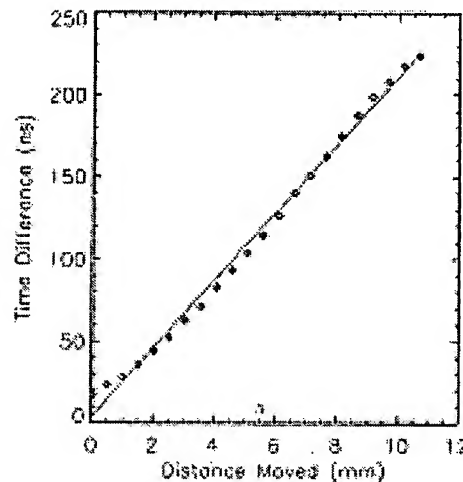
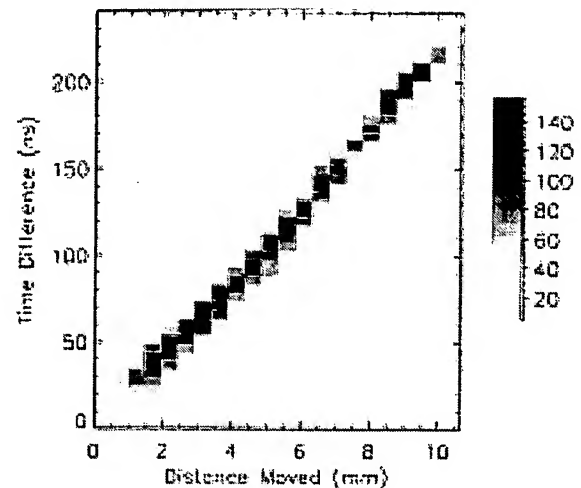


Fig. 6. A fan beam scanned across the side of the detector from the lithium side to the boron side. The  $x$  axis is the actual position of the source on the translation table and  $y$  axis is the depth of the interaction determined by taking the time difference in charge collection. The lower left hand corner corresponds to the front of the lithium face and the upper right hand corner to the front of the boron face. The bottom plot shows the location of the centroid for each position and a linear regression of the centroids. The error on the centroid is less than the diameter of the points.

line. One boron strip in the middle of the detector was selected and the time difference for each position was plotted (see Fig. 6).

Based on a linear regression of the centroids for each position, the detector is shown to have an integral nonlinearity of 5.7% across the detector. This slight nonlinearity is probably due to changes in the electric field near the electrode structures on the faces.

The time resolution of the system for the fan beam illuminating one position on the side of the detector is 14-ns full width half maximum (FWHM). This corresponds to 0.70 mm for this detector. The gamma-ray beam is 0.15 mm wide at the edge of the detector and the average electron motion at this energy is 0.1 mm. Subtracting these contributions in quadrature from the overall resolution of 0.70 mm yields a depth resolution of  $0.68 \pm 0.09$ -mm FWHM.

#### IV. SINGLE-DETECTOR COMPTON TELESCOPE

Having three-dimensional (3-D) readout of a germanium strip detector gives good position resolution in all three dimensions and excellent energy resolution. This allows one to use a single detector as a Compton telescope, as opposed to the traditional configuration using two separate detectors in coincidence to measure two interactions.

Consider gamma-rays coming from a point source. Some of these gamma-rays will Compton scatter in one location in the detector and then interact a second time at a second location in the same detector, depositing all of their energy in these two interactions. The Compton scattering angle in the first interaction can then be determined from the Compton formula

$$\cos \theta = 1 - \left( \frac{m_e c^2}{E_1 + E_2} \right) \left( \frac{E_1}{E_2} \right) \quad (1)$$

where  $\theta$  is the Compton scattering angle,  $m_e$  is the electron rest mass, and  $E_1$  and  $E_2$  are the energies in keV deposited at the two interaction points. Knowing the position of the two interaction points can then be used to draw a cone of possible directions from which the gamma-ray source must be located. Drawing enough of these cones and determining the intersection point reconstructs an image of the gamma-ray source.

This experiment was done with a 8.8  $\mu\text{Ci}$   $^{22}\text{Na}$  source placed 41 cm from the boron side of the detector and a 1.3  $\mu\text{Ci}$   $^{137}\text{Cs}$  source 20 cm to the left of the  $^{22}\text{Na}$ . The data was acquired for 45 minutes. Events that had two strips with signals on the boron side and two strips hit on the lithium side that added up to either 662 keV or 511 keV were selected. These events were then checked to make sure that each hit on the boron side had an exact energy match with a strip on the lithium side and that events were not in neighboring strips. This data set was then used to reconstruct the image using a simple ring sum algorithm.

Each point on a plane located 41 cm from the detector was tested to see if it satisfied the Compton scattering formula within errors using the position and energy information from the event. Each pixel that satisfied these requirements was given a value weighted by the total number of pixels for each event. This was done for both orderings of the event since the true ordering is not always known. All events were then summed together, which produced the image shown in Fig. 7. A similar image was produced when knowledge of the sources positions were used to determine the correct event ordering.

Both sources are visible in the image and are separated by 20 cm. The  $^{137}\text{Cs}$  has better angular resolution because it has the higher gamma-ray energy. The position resolution is about 5 cm, which corresponds to  $7^\circ$  angular resolution. This image would have been impossible without the depth resolution because the interaction point would only have been defined by the overlapping front and back strips.

#### V. TIMING METHODS

All of the experiments in the previous section used the electronics diagrammed in Fig. 2. The TDCs were started by the CFD signals from our custom NIM boards and stopped by a delayed copy of the LED. To determine if the depth resolution measured in the preceding sections is limited by the detector or the

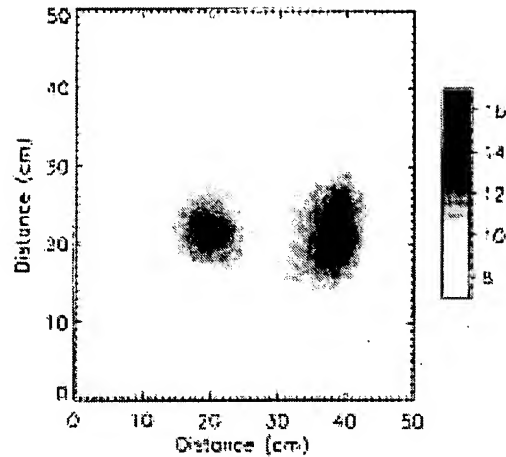


Fig. 7. A reconstructed image of a  $^{137}\text{Cs}$  and  $^{22}\text{Na}$  source placed 41 cm from the boron face of the detector and separated by 20 cm. A Compton ring for each event was drawn at a distance of 41 cm from the front face of the detector and summed together to produce this image.

electronics, the depth resolution was measured using different electronics setups. Commercial NIM modules were used to test these other timing methods due to their flexibility and ease of wiring. Due to channel limitations, only one lithium strip and three boron strips were instrumented.

The CFDs implemented on our custom boards could be limiting the timing resolution of the system. To determine if this is the case, preamplifier signals were fed into Ortec timing filter amplifiers (TFA) set to 200 ns differentiation and integration time. The TFAs signal is sent to an Ortec CFD with 150 ns of external delay. The timing signals from the CFDs start the TDC channels, gate the ADCs, and, after being delayed, stop the TDC. To measure the timing resolution of this system, a  $^{57}\text{Co}$  fan beam illuminated a fixed position on the side of the detector which was 4.5 mm from the lithium face. This beam illuminated all of the horizontal boron strips and, due to attenuation, the first few lithium vertical strips. Using this electronics setup, the timing resolution was 9 ns, which corresponds to 0.45-mm depth resolution. Taking into account the beam width and electron motion, this system has a depth resolution of  $0.41 \pm 0.08$  mm, which is better than the  $0.68 \pm 0.09$ -mm resolution with the CFDs on our custom boards. The lower performance of the custom build electronics is probably due to jitter or noise in the design. Further tests will need to be done to determine the exact cause of the problem.

Replacing the Ortec CFDs with LEDs and setting the triggering threshold to 20 keV resulted in a timing resolution of 9-ns FWHM as well. A comparison of the depth resolution for this configuration and for the configuration with the custom built NIM modules is shown in Fig. 8.

The LED worked as well as the CFD for the 122 keV gamma-ray line but it is not known at this point if it would have the same resolution at a range of different energies. There are many other methods to determine timing accurately without the need for a delay line. One that we have implemented and will be testing soon uses a comparator to look at the crossing between the fast shaped preamplifier signal and the integral of the fast-shaped signal [7]. This timing circuit has been

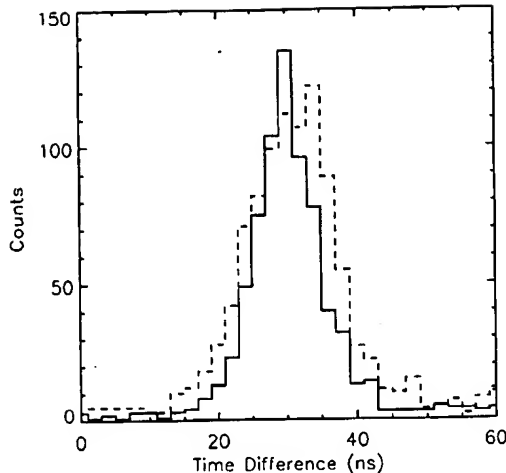


Fig. 8. The solid curve is the time difference between charge collection on the boron and lithium sides of the detector using a LED to determine timing. The dashed curve is the time difference using the integrated NIM electronics used for the other experiments.

produced in CMOS which would be useful for producing an ASIC that combines a shaped signal and timing information for an entire detector. All of these methods will be investigated further at a variety of energies.

#### VI. MULTIPLE INTERACTIONS

As the gamma-ray energy increases, the likelihood of the gamma-ray depositing all of its energy in one pixel decreases. At a gamma-ray energy of 662 keV from a  $^{137}\text{Cs}$  source, the photo-peak efficiency in the germanium detector is less than 1%. The rest of the events will involve Compton scattering and charge sharing with neighboring strips. Depth information should be able to distinguish between these two types of events. This would allow charge sharing events to be used in event reconstruction using the average position and the sum of the energies in the two strips. The Compton scattering events would then be available for reconstruction. This increases the efficiency of the detector by allowing more event types to be used in the final analysis.

To look at depth information in neighboring strips, a  $^{137}\text{Cs}$  source was placed 41 cm from the detectors boron side. Events were selected that had only one signal on the boron side and two neighboring strips hit on the lithium side. The time difference between the two neighboring strips on the lithium side was histogrammed. Charge sharing events should have essentially no time difference and Compton events should have a variety of time differences based on where the interactions occurred. Charge sharing events should be independent of source position while Compton scattering should be affected by source location because this movement causes changes in the scattering angles between the strips. This was all seen in the experiment as shown in Fig. 9. There is a center peak, charge sharing events, that was unaffected by source position and then Compton events that shifted with changing source position. More work is necessary

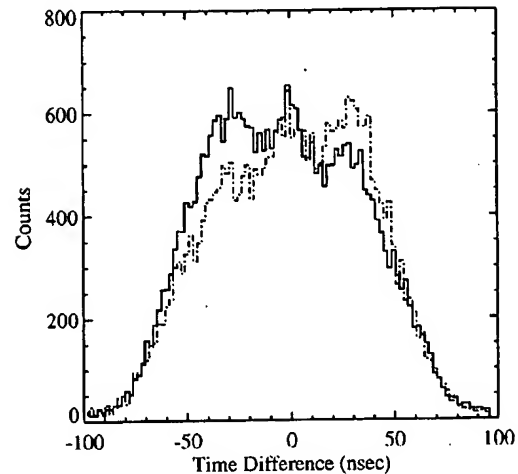


Fig. 9. A  $^{137}\text{Cs}$  source was used to illuminate the detector at two different points separated by 20 cm at a distance of 41 cm from the boron face of the detector. The time difference between neighboring strip hits on the lithium side is histogrammed. The solid line is for the source centered with the detector and the dashed line is for the source located 20 cm above the center.

to make this technique useful for distinguishing between different event types.

#### VII. CONCLUSION

The depth of a gamma-ray interaction can be measured in an orthogonal germanium strip detector to less than 0.5 mm. The depth information coupled with the  $x$ - $y$  position information from the strips yields a detector that is useful for a number of ground and space based instruments. Compton telescopes built from detectors with 3-D readout would have better image and energy reconstruction. Also, this enables the use of thicker detectors which would lead to less electronics for the same amount of detector volume.

#### REFERENCES

- [1] R. A. Kroeger, W. N. Johnson, J. D. Kurfess, R. L. Kinzer, N. Gehrels, S. E. Inderhees, B. Philips, and B. Graham, "Spatial resolution and imaging of gamma-rays with germanium strip detectors," *SPIE*, vol. 2518, pp. 236-243, 1995.
- [2] M. Momayezi, W. K. Warburton, and R. Kroeger, "Position resolution in a ge-strip detector," *SPIE*, vol. 3768, pp. 530-537, 1999.
- [3] M. Amman and P. N. Luke, "Three-dimensional position sensing and field shaping in orthogonal-strip germanium detectors," *Nucl. Instrum. Methods*, vol. A452, pp. 155-166, 2000.
- [4] J. M. Links and L. S. Graham, *Nuclear Medicine: Technology and Techniques*, 4th ed, D. R. Bernier, P. E. Christian, and J. K. Langan, Eds. St. Louis, MO: Mosby, 1997, pp. 56-97.
- [5] K. Vetter, A. Kuhn, M. A. Deleplanque, I. Y. Lee, F. S. Stephens, G. J. Schmid, D. Beckedahl, J. J. Blair, R. M. Clark, M. Cromaz, R. M. Diamond, P. Fallon, G. J. Lane, J. E. Kammeraad, A. O. Macchiavelli, and C. E. Svensson, "Three-dimensional position sensitivity in two-dimensionally segmented hp-ge detectors," *Nucl. Instrum. Methods*, vol. A452, pp. 223-238, 2000.
- [6] G. F. Knoll, *Radiation Detection and Measurement*, 2nd ed. New York: Wiley, 1989, pp. 340-342.
- [7] B. T. Turko and R. C. Smith, "A precision timing discriminator for high density detector systems," *IEEE Trans. Nucl. Sci.*, vol. 39, pp. 1311-1315, Oct. 1992.

# Calibration of a PET Detector Module that Measures Depth of Interaction\*

J. S. Huber, *Member, IEEE*, W.W. Moses, *Senior Member, IEEE*, P. R. G. Virador  
Lawrence Berkeley National Laboratory, University of California, Berkeley, CA 94720

## Abstract

We investigate two *in situ* calibration techniques (using gamma rays incident from the patient side) for PET detector modules that measure interaction depth via an analog ratio. For each crystal element in the camera, we need to determine two unknowns: the gain ratio  $K$  of the two detector (PMT and PD) signals and the depth dependence  $\alpha$  of the signals (defined as the ratio of the signal observed when the crystal is excited at the end closest to and furthest from the detector). The light collection is assumed to be linearly dependent on distance from the detector end, in agreement with experimental results. The first method extracts  $K$  and  $\alpha$  using (a) the ratio of the PMT and PD signals for interactions that occur in the detector end closest to the patient (the most probable depth) and (b) the shape of the PMT pulse height distribution which reflects the exponential attenuation length in the detector. The second method utilizes the fact that  $E = PD + PMT$  (the total energy estimator) is independent of  $\Gamma = PD/(PD + PMT)$  (the depth estimator) when  $K$  is correct, with a distribution position that is  $\alpha$  dependent. On simulated data, both the gain ratio and depth dependence are determined with errors of 3% rms and 2% rms respectively, resulting in minimal degradation of energy and depth resolution.

## I. INTRODUCTION

We have previously described the design for a PET detector module that consists of an array of LSO crystals coupled on one end to a photomultiplier tube and on the opposite end to an array of silicon photodiodes [1]. We calibrated this prototype detector module using an electronically collimated beam of annihilation photons incident from the side of the detector to excite at a specified depth of interaction (figure 1a). Others have suggested calibrating different depth-encoding PET detectors using techniques similarly dependent on measurements with side incident beams to provide a photopeak pulse height versus depth look-up table [2-3]. However, using side incident gamma rays is awkward for complete cameras since recalibration is only possible by removing detectors from the gantry.

We therefore investigate *in situ* calibration techniques (*i.e.* those that utilize only gamma rays incident from the patient side of the detector module such as in figure 1b). We use a Monte Carlo simulation that includes the measured electronic noise, energy resolution, and signal levels, as well as energy dependent Compton and photoelectric cross sections in LSO.

\* This work was supported in part by the U.S. Department of Energy under Contract No. DE-AC03-76SF00098, in part by Public Health Service Grant Nos. P01-HL25840 and R01-CA67911, and in part by Breast Cancer Research Program of the University of California Grant No. 1RB-0068.

The light collection is assumed to be linearly dependent on the distance of interaction from the photodetector, which has been empirically found to be a good approximation [1]. More precisely, the PD and PMT signals (in ADC counts) for an ideal detector are given as a function of depth  $x$  by:

$$PD(x) = \frac{E}{\alpha} k_{pd} [(\alpha - 1) (1 - \frac{x}{L}) + 1] \quad (1)$$

$$PMT(x) = \frac{E}{\alpha} k_{pmt} [(\alpha - 1) \frac{x}{L} + 1] \quad (2)$$

where  $k_{pd}$  and  $k_{pmt}$  are the gain factors that convert energy deposition to ADC counts for each photodetector,  $E$  is the energy deposited in the crystal,  $L$  is the crystal length, and  $\alpha$  is the depth dependence (defined as the ratio of the signal observed when the crystal is excited at the end closest to and furthest from the photodetector). Depth  $x$  is defined to be 0 at the PD end. Figure 2 shows these detector signals as a function of depth for an ideal detector, assuming noise free readout, perfect energy resolution, and monoenergetic energy deposition.

The necessary calibration parameters are depth dependence ( $\alpha$ ) and the relative gain of the PMT and PD ( $K$ ). More specifically,

$$\alpha \equiv \frac{PMT(x=L)}{PMT(x=0)} = \frac{PD(x=0)}{PD(x=L)} \quad (3)$$

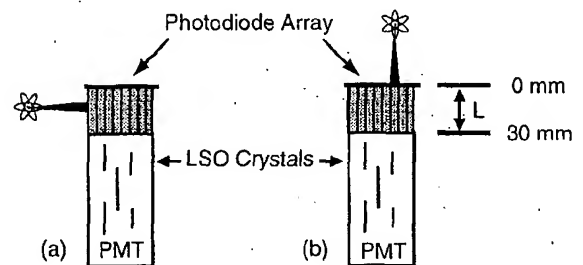


Figure 1: Calibration geometry for a depth of interaction detector module. An electronically collimated beam of annihilation photons are incident from (a) the side of the detector module to excite at a specified depth of interaction or (b) the patient side of the detector module for *in situ* calibration.

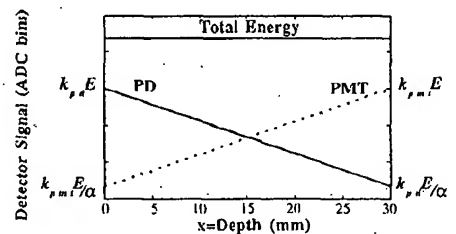


Figure 2: The PD and PMT detector signals, which are linearly dependent on the depth of interaction ( $x$ ) from the photodetector. The depth  $x$  is defined to be 0 at the PD photodetector. Total energy is the sum of PD and PMT.

$$K \equiv \frac{k_{pmt}}{k_{pd}} = \frac{PMT(x=L)}{PD(x=0)} = \alpha \frac{PMT(x=0)}{PD(x=0)}. \quad (4)$$

In this paper we present two different *in situ* calibration methods used to extract  $K$  and  $\alpha$  for a single crystal element.

## II. SIMULATION

Monte Carlo data are used to simulate the performance of a single LSO crystal coupled on one end to a silicon photodiode and on the opposite end to a photomultiplier tube. Normally incident 511 keV photons enter the crystal on the PD end and interact in the crystal via Compton scattering and/or photoelectric absorption, assuming energy dependent cross sections in LSO. A 1.2 cm attenuation length ( $1/\mu$ ) of LSO is assumed [4]. Since there is only a single simulated crystal, Compton scattered photons that escape the crystal are lost and none are added from neighboring crystals.

The photodetectors are assumed to have a quantum efficiency of 0.8 and 0.2 for the PD and PMT, respectively. The detected signal is smeared by a Gaussian distribution to simulate the effect of finite scintillator energy resolution. The rms width of the Gaussian is proportional to the square-root of the signal and the proportionality constant is chosen to match observed energy resolution in LSO. This scintillator based "noise" is summed in quadrature with the measured electronic noise (190 electrons rms for PD and 0 for PMT detector). The signal in terms of energy is multiplied by the gain factor  $k_{pd}$  (or  $k_{pmt}$ ) to give the signal PD (or PMT) in terms of ADC bins. We want to extract the relative gain  $K$  and calibrate so that 1 PMT ADC bin equals 1 PD ADC bin after correction. With these assumptions, the total energy resolution at 511 keV is ~19% fwhm; this is pessimistic compared to the expected detector performance [1]. Calibration results extracted with a better energy resolution are found not to affect the results.

## III. EXPONENTIAL ATTENUATION METHOD

The light collection is linearly dependent on the depth. Thus, the exponential nature of annihilation photon interaction in the crystal is reflected as an exponential shape of the PMT and PD pulse height spectra. The first calibration method that we describe utilizes this exponential shape.

Figure 3 demonstrates the underlying data that is used for the calibration. Consider 511 keV gammas that interact only via photoelectric effect in a noise free detector. Interactions at a single depth would appear as a delta function in the pulse height distribution. As the distribution of interaction depths is exponential (due to exponential attenuation in LSO), the PD and PMT pulse height spectra also have exponential slopes. The PMT spectrum has a clear peak at low pulse height bins, corresponding to interactions at the patient end of the scintillation crystal ( $x=0$ , the most probable depth). Because of light sharing, interactions at  $x=L$  (i.e. close to the PMT) populate high pulse height bins. Ideally, we could use the four edges of the spectra —  $PD(x=0)$ ,  $PD(x=L)$ ,  $PMT(x=0)$  and

$PMT(x=L)$  — to extract the calibration constants using equations (3) and (4).

For a realistic detector that includes electronic noise, finite energy resolution, and Compton scatter (as in figure 4), we can still identify the peaks corresponding to interactions at  $x=0$ . However, it becomes difficult to accurately identify the pulse height edges for the  $x=L$  interactions. Thus, we have developed an algorithm to determine  $K$  and  $\alpha$  using the  $x=0$  peaks and the shape of the PMT spectrum.

For a realistic detector, Gaussian smearing of the PMT pulse height spectrum rounds off the abrupt edges seen at  $x=0$  and  $x=L$  in figure 3 and alters the exponential shape near these  $x$  values. However, the shape is unaffected for  $0.1L \leq x \leq 0.9L$ . Thus the PMT pulse height spectrum is fit with an exponential over a limited region — from 5% above the  $x=0$  peak to 25% below the bin where the PMT spectrum tail first goes to zero — in order to extract the slope  $m$  ( $N = N_0 \exp(-b - mPMT) = N_0 \exp(-x/\mu)$ ). The  $PMT(x=0)$  peak is estimated by the ADC bin with the maximum number of events. The combination of the peak  $PMT(x=0)$  and exponential slope  $m$  are used to extract alpha:

$$\alpha = 1 + \frac{L}{m \mu PMT(x=0)}. \quad (5)$$

The PD pulse height spectrum peaks for interactions corresponding to  $x=0$ , which is also estimated by the ADC bin with the maximum number of events. We can then obtain the relative gain factor  $K$  from  $PMT(x=0)$  and  $PD(x=0)$  using equation (4).

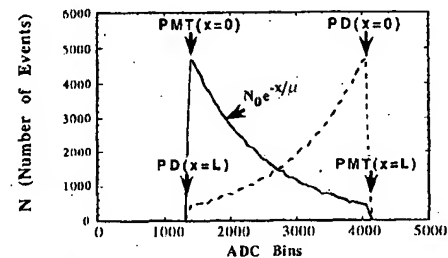


Figure 3: The PMT and PD distributions simulated with  $\alpha=3$  and  $K=1$  for an ideal detector. Exponential attenuation ( $1/\mu$ ) is evident for both PD and PMT distributions, as well as the edges corresponding to  $x=0$  and  $x=L$ .

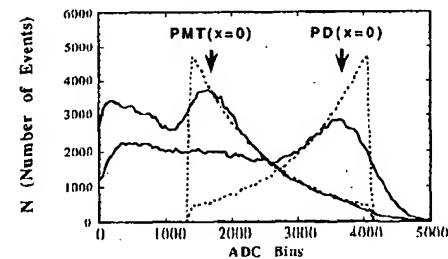


Figure 4: The PMT and PD distributions simulated with  $\alpha=3$  and  $K=1$  for a realistic (solid lines) and ideal (dashed lines) detector. Exponential attenuation ( $1/\mu$ ) is evident for the realistic PMT distribution (to the right of its peak), as well as the edges corresponding to  $x=0$ .



We need to correct for systematic errors, such as those caused by the  $\text{PMT}(x=0)$  and  $\text{PD}(x=0)$  peak finding algorithm (see figure 4). To obtain these correction factors, a data set of 20 runs is simulated with different  $(\alpha, K)$  combinations and 200k events per run. The true (*i.e.* input)  $\alpha$  and  $K$  constants range in value from 2–4 and 0.5–1.5 respectively to fully cover the expected detector conditions. The nominal values are  $\alpha=3$  and  $K=1$ . This calibration data set is used to measure “raw values” of  $\alpha$  and  $K$  with the exponential attenuation method described above. We plot the measured raw versus true values and fit a line for both  $\alpha$  and  $K$ , providing correction factors for future data sets.

To estimate the errors in this method, a second data set of 20 runs is simulated with 200k events each and the same  $(\alpha, K)$  combinations as in the calibration data set but with different random seeds. The exponential attenuation method is applied to each run, then corrected with the corresponding  $\alpha$  or  $K$  calibration line. Figure 5 shows the resulting measurements for  $\alpha$  and  $K$  as a function of the true values. A line of slope 1 is also shown to represent the desired values. Thus, we obtain  $\alpha$  with a 3% rms error and  $K$  with a 2% rms error using this method. In figure 6, the pulse height spectra and depth of interaction distributions are shown to be almost indistinguishable when using either the true or measured calibration constants. When exciting at a fixed depth, we also see little difference in the depth distributions for true and measured calibration constants. Therefore, we have found that the calibration errors cause only a minute degradation of the energy and depth resolution.

This technique uses only a crude estimation of the pulse height peaks ( $\text{PMT}(x=0)$  and  $\text{PD}(x=0)$ ) by using the bin with the maximum number of events for each photodetector. Clearly a more sophisticated fit for the peak region would give a better estimation. In addition, the PMT spectrum should be fit with an exponential after the Compton background has been subtracted. However, our investigation showed accurate slope extraction when fitting without subtraction. For speed and simplicity, we choose not to fit the peaks or subtract off the background since they aren't necessary. A run of 200k events is a very large sample when considering that we have over 20k crystals in need of calibration in our proposed PET camera. However, preliminary measurements (with 20k events per run) indicate that this technique will yield acceptable results even with a smaller number of events. Acquisition time for sufficient data to perform calibration is approximately 10 minutes (assuming 30k crystals, 20k events/crystal, and 1 MHz acquisition rate). Computer analysis (histogramming, fitting, and extracting constants) is expected to take approximately 1.5 hours on a typical UNIX workstation.

#### IV. CONSTANT ENERGY SUM METHOD

Assuming the light collection to be linearly dependent on depth, the second calibration method utilizes the fact that the total energy estimator ( $E=\text{PD}+\text{PMT}$ ) is independent of the depth estimator ( $\Gamma=\text{PD}/(\text{PD}+\text{PMT})$ ) if the relative gain  $K$  is

correct. Figure 2 shows the PD, PMT, and total energy detector signals as a function of true interaction depth for an ideal detector with a correct relative gain of 1. Figure 7 shows the total energy as a function of the depth estimator for an ideal detector with either  $K=1$  (figure 7a) or  $K=1.5$  (figure 7b). A clear dependence on  $\Gamma$  is observed when the gain is incorrect, whereas the total energy is flat when the gain is correct. Thus we can estimate  $K$  from the slope of  $E$  as a function of  $\Gamma$ . Figure 7 also shows that the total energy position is a function of the calibration constants; the line is centered for correct gain (figure 7a) and shifts to the left for  $K>1$  (figure 7b). More precisely, the upper edge is given by

$$\Gamma(x=0) = \frac{\alpha}{\alpha+K} \quad (6)$$

Thus we can extract the calibration constant  $\alpha$  by measuring the upper edge  $\Gamma(x=0)$  once we have determined  $K$ .

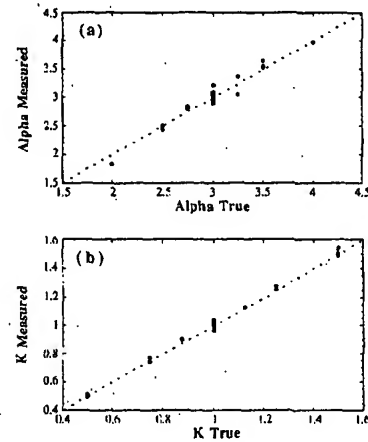


Figure 5: The correlation between true and measured calibration constants using the exponential attenuation method for (a)  $\alpha$  and (b)  $K$ . The lines of slope 1 represent the desired values.

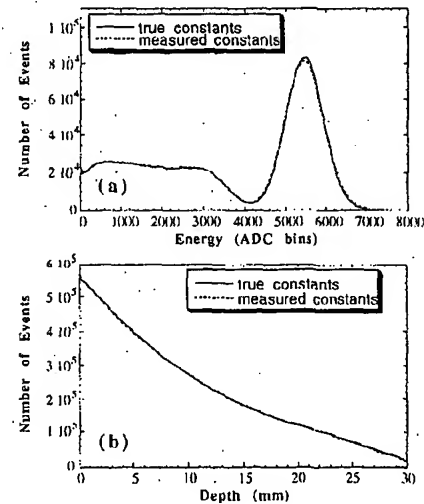


Figure 6: The (a) total energy pulse height spectrum and (b) depth of interaction distribution for both the true and measured calibration constants. The curves are almost indistinguishable.



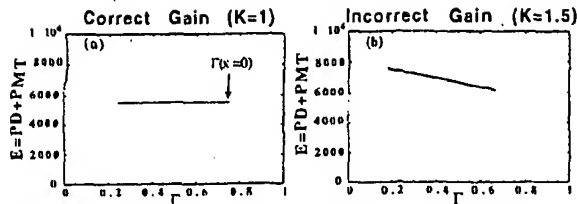


Figure 7: The total energy estimator  $E=PD+PMT$  as a function of the depth estimator  $\Gamma=PD/(PD+PMT)$  for an ideal detector with  $\alpha=3$  and (a) a correct relative gain of  $K=1$  or (b) an incorrect gain of  $K=1.5$ . Total energy is independent of  $\Gamma$  if the gain is correct.

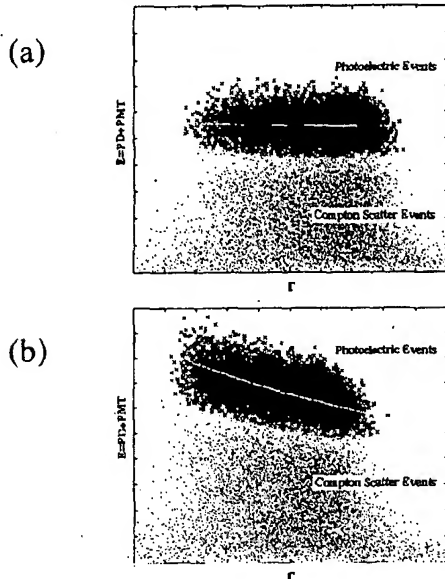


Figure 8: The total energy estimator  $E=PD+PMT$  as a function of the depth estimator  $\Gamma=PD/(PD+PMT)$  for a realistic detector with  $\alpha=3$  and (a) a correct relative gain of  $K=1$  or (b) an incorrect gain of  $K=1.5$ . Total energy is independent of  $\Gamma$  if the gain is correct. The crosses indicate photoelectric events and the dots are Compton scatter events, as determined by an expectation maximization technique. The white lines are a fit of only photoelectric events (used to extract  $K$ ).

For a realistic detector that includes electronic noise, finite energy resolution and Compton scatter, the lines in figure 7 become a scatter plot of  $E$  versus  $\Gamma$  but still demonstrate independence of  $\Gamma$  if the gain is correct (figure 8). Figure 8 also shows an excellent separation between photopeak and Compton scatter events for both correct and incorrect gains. In order to properly extract  $K$  from the scatter plot for a realistic detector, we select only the photopeak events using an expectation maximization technique [5]. We model the probability densities of the events in the variables  $\Gamma$  and  $E$  as a mixture of two Gaussian functions and classify each event according to Bayesian inferencing [6]. The white line in figure 8b, corresponding to the average  $E$  as a function of  $\Gamma$  for photopeak events only, is a hyperbola. Thus rather than fitting  $E$ , we make a linear fit of the inverse of  $E$ . We extract  $K$  from the slope and intercept of this line, giving an excellent fit for photopeak events as seen in figure 8. We are able to observe a

clear upper edge  $\Gamma(x=0)$  for all  $K$  values. This edge is determined by histogramming  $\Gamma$  and estimating the peak by the bin with the maximum number of events. We can then determine  $\alpha$  from both  $K$  and  $\Gamma(x=0)$  using equation (6).

The same calibration data set used to measure  $\alpha$  and  $K$  with the exponential attenuation method (described previously) is used for the constant energy sum method. However, only the first 20k events per run are used because of the computation time required by the expectation maximization algorithm. There are systematic errors such as the position of the  $\Gamma(x=0)$  peak, but the calibration results show a correlation between the measured raw values and the true values. We plot the measured raw versus true values and fit a line for both  $\alpha$  and  $K$ , providing correction factors for future data sets.

In order to estimate the errors, the constant energy sum method is applied to the same test data set used for the exponential attenuation method but using only the first 20k

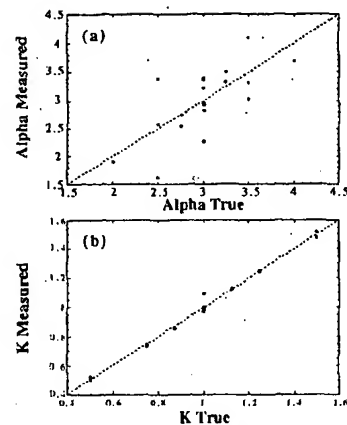


Figure 9: The correlation between true and measured calibration constants using the constant energy sum method for (a)  $\alpha$  and (b)  $K$ . The lines of slope 1 represent the desired values.

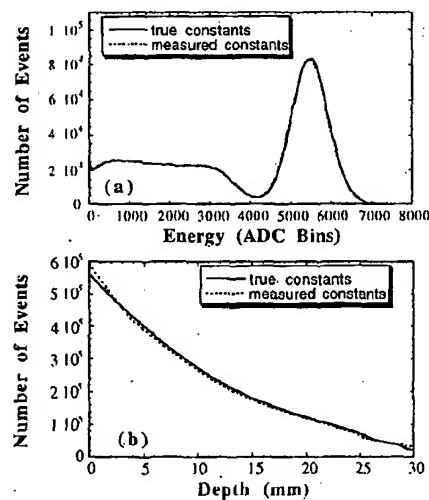


Figure 10: The (a) total energy pulse height spectrum and (b) depth of interaction distribution for both the true and measured calibration constants. Excellent agreement is seen.

events. These measured raw values of  $\alpha$  and  $K$  are then corrected with the corresponding  $\alpha$  or  $K$  calibration line. Figure 9 shows the resulting measurements for  $\alpha$  and  $K$  as a function of the true values. Thus, we obtain  $\alpha$  with a 14% rms error and  $K$  with a 4% rms error using this method. Although the rms error for  $\alpha$  is much larger for this method when compared to the previous method (with 2% rms for  $\alpha$ ), the calibration errors cause only a minimal degradation of the energy and depth resolution (figure 10). For the results reported here, automated Matlab code was used to perform the calculations and it took approximately 2 minutes to calibrate each crystal (i.e. 20k events). Since running loops within Matlab is known to be very slow, an automated version in C is expected to be significantly faster. We anticipate that the constant energy sum method will be ~2 times slower than the previous method (i.e. ~3 hours for 30k crystals).

## V. DISCUSSION

These results are based on a single simulated crystal. One cannot truly validate a detector calibration method or select among competing options without having constructed a number of functioning detector modules, since presently unmodeled effects (such as Compton scatter from adjacent crystals, deviations from linear dependence of the light collection on depth, electrical and optical crosstalk between detector elements, etc.) may need to be accounted for. However, the concepts presented herein appear promising and practical based on this relatively simple model.

Although we have assumed the light collection to be linearly dependent on depth for these methods (in agreement with experiment), they could easily be modified for a different depth dependence as long as the functional form is known; this can be determined using measurements with side incident gamma rays. Calibration techniques are by necessity detector specific and so it is difficult to accurately assess whether these methods can be used with other detector designs. However, there are several current designs [2,3,7,8] that measure depth with an analog signal (or signals) whose amplitude depends on depth. Requiring the depth distribution to be consistent with the known exponential distribution should be sufficient to calibrate those with one analog signal, while requiring an additional constraint (i.e. requiring the sum to be depth independent or identifying interactions that occur at the crystal boundaries) should be sufficient for those that employ a ratio.

## VI. CONCLUSIONS

We investigate two *in situ* calibration techniques for PET detector modules that measure depth via an analog ratio. The first method uses the ratio of the detector signals at the most probable depth as well as the exponential shape of the PMT pulse height spectrum in order to extract the calibration constants. We obtain the depth dependence ( $\alpha$ ) with a 3% rms error and the relative detector gain ( $K$ ) with a 2% rms error using this exponential attenuation method. In the second method we select photopeak events and fit the total energy versus depth estimator ( $\Gamma$ ) shape to extract  $K$ ; we then

determine  $\alpha$  from both  $K$  and the upper edge  $\Gamma(x=0)$ . We obtain the depth dependence with a 14% rms error and the relative detector gain with a 4% rms error using this constant energy sum method. Estimated calibration times are 2-3 hours for a 30,000 crystal tomograph, dominated by fitting time. The larger errors in the constant energy sum method may be due to the smaller number of events (20k vs. 200k). However, both calibration techniques cause only minimal degradation of the energy and depth resolution so they are both viable options for *in situ* calibration.

## VII. ACKNOWLEDGMENTS

We wish to acknowledge the substantial contribution of Mr. Jonathan Maltz to the development of the constant energy sum method. This work was supported in part by the Director, Office of Energy Research, Office of Biological and Environmental Research, Medical Applications and Biophysical Research Division of the U.S. Department of Energy under contract No. DE-AC03-76SF00098, in part by the National Institutes of Health, National Heart, Lung, and Blood Institute, National Cancer Institute, and National Institute of Neurological Disorders and Stroke under grants No. P01-HL25840 and R01-CA67911, and in part by the Breast Cancer Fund of the State of California through the Breast Cancer Research Program of the University of California under grant No. 1RB-0068.

## VIII. REFERENCES

- [1] J.S. Huber, W.W. Moses, et al., "Characterization of a 64 Channel PET Detector Using Photodiodes for Crystal Identification," *IEEE Trans. Nucl. Sci.*, vol. NS-44, pp. 1197-1201, 1997.
- [2] J.G. Rogers, C. Moisan, et al., "A Practical Block Detector for a Depth-Encoding PET Camera," *IEEE Trans. Nucl. Sci.*, vol. NS-43, pp. 3240-3248, 1996.
- [3] J.L. Robar, C.J. Thompson, et al., "Construction and calibration of detectors for high-resolution metabolic breast cancer imaging," *Nucl. Instr. and Meth. in Phys. Res.*, vol. A 392, pp. 402-406, 1997.
- [4] C.L. Melcher and J.S. Schweitzer, "Cerium-doped lutetium orthosilicate: A fast, efficient new scintillator," *IEEE Trans. Nucl. Sci.*, vol. NS-39, pp. 502, 1992.
- [5] A.P. Dempster, N.M. Laird, et al., "Maximum Likelihood from Incomplete Data via the EM Algorithm," *Journal of the Royal Statistical Society, B* 39, pp. 1-38, 1977.
- [6] C. Bishop, *Neural Networks for Pattern Recognition*, 1996, pp. 59-73.
- [7] R. Miyaoka, T.K. Lewellen, et al., "Design of a Depth of Interaction (DOI) PET Detector Module," *submitted to IEEE Trans. Nucl. Sci.*, vol. NS-45, 1998.
- [8] Y. Shao, S.R. Cherry, et al., "A Study of Depth of Interaction with Multi-Anode PMT and Single Channel Photodiode," *submitted to IEEE Trans. Nucl. Sci.*, vol. NS-45, 1998.

[Home](#)[Search](#)[Journals](#)[Abstract Databases](#)[Reference Works](#)[My Alerts](#)[My Profile](#)[Help](#)Quick Search:  within   [? Search tips](#)16 of 57 [results list](#) [◀ previous](#) [next ▶](#)**Nuclear Instruments and Methods in Physics Research Section A: Accelerators, Spectrometers, Detectors and Associated Equipment**Volume 242, Issue 3, 15 January 1986, Pages 443-449doi:10.1016/0168-9002(86)90443-2 [? Cite or link using doi](#)

Copyright © 1986 Published by Elsevier Science B.V.

**This Document**▶ **Abstract**

- [Abstract + References](#)
- [PDF \(416 K\)](#)

**Section III. Models and data analysis****Parallel pulse processing for mercuric iodide gamma-ray detectors<sup>\*1</sup>****A. Beyerle, V. Gerrish and K. Hull**

EG&amp;G Energy Measurements, Inc., Santa Barbara Operations, Goleta, California 93117, USA

Available online 14 October 2002.

**Actions**

- [Cited By](#)
- [Save as Citation Alert](#)
- [E-mail Article](#)
- [Export Citation](#)

**Abstract**

Mercuric iodide, a high-Z, wide band-gap semiconductor material, is a room temperature gamma-ray detector. Poor hole transport properties limit the detector performance. By parallel pulse processing schemes we are exploring this problem and making corrections to enhance resolution. This yields interaction depth information which is used to estimate hole collection deficits. Deficit estimates are used as corrections to pulse height to enhance resolution, or to reject pulses from high-deficit regions. These techniques have been implemented by several schemes for filtering the pulses using off-the-shelf amplifiers and computer simulation of amplifiers on detectors from 1–3 mm thick. Hardware and simulated results are compared and improved spectral performance is discussed. A resolution better than 7% for correction and 2.5% for rejection of hole deficit is obtained.

<sup>\*1</sup> This work was performed under the auspices of the US Department of Energy under Contract No. DE-AC08-83NV10282.

**Nuclear Instruments and Methods in Physics Research Section A: Accelerators, Spectrometers, Detectors and Associated Equipment**  
Volume 242, Issue 3, 15 January 1986, Pages 443-449

**This Document**▶ **Abstract**

- [Abstract + References](#)
- [PDF \(416 K\)](#)

**Actions**

- [Cited By](#)

# Spectroscopic-Grade X-Ray Imaging up to 100-kHz Frame Rate With Controlled-Drift Detectors

Andrea Castoldi, *Member, IEEE*, Chiara Guazzoni, *Member, IEEE*, Pavel Rehak, *Member, IEEE*, and Lothar Strüder

**Abstract**—Controlled-drift detectors are fully depleted silicon detectors for X-ray imaging that combine good position resolution with very fast frame readout. The basic feature of the controlled-drift detector is the transport of the charge packets stored in each pixel column to the output electrode by means of a uniform drift field. The drift time of the charge packet identifies the pixel of incidence. Images of an X-ray source obtained with the controlled-drift detector up to 100-kHz frame rate are presented and discussed. The achievable energy resolution as a function of the operating temperature and frame rate is analyzed.

**Index Terms**—Controlled-drift detector, fast readout, X-ray imaging.

## I. INTRODUCTION

THE controlled-drift detector (CDD) was proposed in 1997 [1], and the first experimental evidence of its working principle was reported in [2]. The device is built on a fully depleted 300- $\mu\text{m}$ -thick high-resistivity wafer and is operated in integrate-readout mode. The basic idea of the CDD is to generate columns of equally spaced potential wells for the electrons by superposing a periodic perturbation of sufficient amplitude to a linear drift potential. During the integration mode, the signal electrons are stored within these wells. The removal of these potential barriers in an externally controlled way allows the use of the linear drift potential to sweep the electrons toward the readout electrodes. The time between the removal of the barriers and the arrival of the signal electrons at the readout electrodes gives the position of the irradiated pixel along the drift direction. The second coordinate is obtained by providing a separate readout electrode for each pixel column. Arrays of deep  $p$ -implants provide lateral confinement. In Fig. 1, the layout of the anode region of the controlled-drift detector is shown.

This readout mechanism is inherently faster than the clocked transfer of the rows of pixels toward the readout section typical of the pn charge-coupled device (CCD) because now charge transfer and signal processing are carried out simultaneously. The frame rate in the CDD is ultimately limited by the

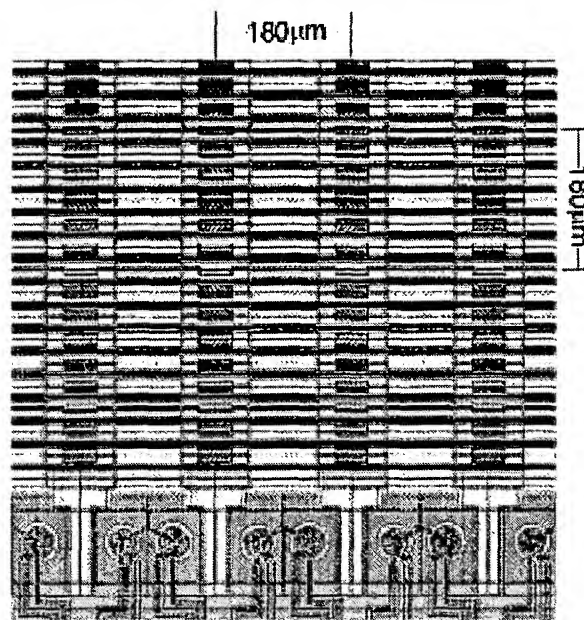


Fig. 1. Layout of the anode region of the controlled-drift detector. The pixel size is also indicated.

electron drift time, which is typically 2–6  $\mu\text{s}$  for 1-cm-long device depending on the applied drift field. The advantage of this readout mechanism is twofold: 1) a higher frame rate with respect to the fully depleted pn-CCD [3], which represents the reference device for high-resolution imaging and spectroscopy of X rays, and 2) a lower contribution of the thermal noise due to a shorter integration time, leading to high energy resolution.

We performed the first extended test of the imaging and spectroscopic capability of the CDD by irradiating a column of the detector at room temperature. The aim of the measurements was twofold: 1) verify the proper operation of the CDD at frame frequencies close to the limiting value set by the electron drift time and 2) verify the expected improvement of the energy resolution with the frame frequency. In Section II, we present the images of a  $^{55}\text{Fe}$  source obtained with the CDD at different frame rates up to 100 kHz. In Section III, the achievable energy resolution is discussed as a function of the frame rate and of the operating temperature.

## II. X-RAY IMAGING

One column of the detector has been irradiated with a  $^{55}\text{Fe}$  source to verify the imaging capability, the maximum frame

Manuscript received November 3, 2000; revised February 19, 2001. This work was supported by Istituto Nazionale di Fisica Nucleare, Sezione di Milano, and by the U.S. Department of Energy under Contract DE-AC02-98CH10886.

A. Castoldi is with the Dipartimento di Ingegneria Nucleare Ce.S.N.E.F., Politecnico di Milano, Milano 20133, Italy, and INFN, Sezione di Milano, Milano, Italy (e-mail: Andrea.Castoldi@polimi.it).

C. Guazzoni is with the Dipartimento di Elettronica e Informazione, Politecnico di Milano, Milano 20133, Italy, and INFN, Sezione di Milano, Milano, Italy (e-mail: Chiara.Guazzoni@mi.infn.it).

P. Rehak is with the Instrumentation Division, Brookhaven National Laboratory, Upton, NY 11973 USA (e-mail: rehak@klee.inst.bnl.gov).

L. Strüder is with the Halbleiterlabor of the Max Planck Institut, München D-81739, Germany (e-mail: lts@hll.mpg.de).

Publisher Item Identifier S 0018-9499(01)06959-3.

rate, and the achievable energy resolution. The pulses delivered by the on-chip JFET (source follower configuration) were fed to a low-noise voltage preamplifier followed by a pseudo-Gaussian shaper (0.25- $\mu$ s shaping time) and an 8-bit digitizer controlled by a PC to acquire the output waveforms, subtract the background (mainly due to thermal generation), and compute the amplitude and the drift time of each pulse. We acquired several images of a  $^{55}\text{Fe}$  source at room temperature for different frame rates. As the detector area is unshielded, the ratio between the integration time and the readout time is typically chosen greater than one in order to limit the number of out-of-time events. In our case, it was set equal to nine in all measurements. With this choice, we tested the CDD up to a 100-kHz frame rate, corresponding to a duration of the readout phase of 1  $\mu$ s. Considering that the electron drift occurs within the first 0.7  $\mu$ s of the readout phase, for the 100-kHz case signal processing was overlapping with the subsequent integration phase.

The operating drift field was 200 V/cm and the amplitude of the surface perturbation was 2 V.

Fig. 2(a) shows the scatter plot energy versus drift time (i.e., position) of the detected events when the CDD is operated at a 10-kHz frame rate. Moving along the time axis, we see that the events are gathered in well-separated clusters centered at about 6 keV (the Mn  $K\alpha$  and Mn  $K\beta$  lines are not resolved), indicating the illuminated pixels. In Fig. 2(b), the scatter plot related to a 30-kHz frame rate operation is reported. As we can see, the clusters relative to the  $K\beta$  line start to separate from the ones corresponding to the  $K\alpha$  line as the energy resolution is improving. In the image taken at a 100-kHz frame rate [Fig. 2(c)], the  $K\alpha$  and  $K\beta$  lines can be clearly distinguished.

A more detailed analysis is obtained by plotting the measured events against one parameter at a time. Fig. 3 shows the distribution of the events along the time axis for the image acquired at a 100-kHz frame rate. The full-width at half-maximum (FWHM) of the peaks is smaller than 15%, leaving a margin for reduction of the pixel size along the drift coordinate (actual size is 180  $\mu$ m).

Fig. 4 shows the total distribution of the event energies (i.e., the spectrum of the  $^{55}\text{Fe}$  source collected by all the pixels) for two different frame rates (10 and 100 kHz).

At a 10-kHz frame rate, the energy resolution at the Mn  $K\alpha$  line (5.899 keV) is 837 eV FWHM, corresponding to an equivalent noise charge (ENC) of 98 electron rms. By increasing the frame frequency, we shorten the integration time and therefore reduce the amount of leakage charge that accumulates in the pixels, thus improving the energy resolution. The energy resolution at 100-kHz frame rate is 339 eV FWHM, corresponding to an ENC of 37 electrons rms.

To further reduce the integration time, we changed the ratio between the duration of the integration and the readout phase. In Fig. 5, the scatter plot energy versus drift time of the detected events when the CDD is operated at a 100-kHz frame rate, with a duration of the integration phase of only 6.7  $\mu$ s. As expected, we obtained a better energy resolution at the Mn  $K\alpha$  line equal to 296 eV FWHM, corresponding to an ENC of 32 electron rms (see Fig. 6).

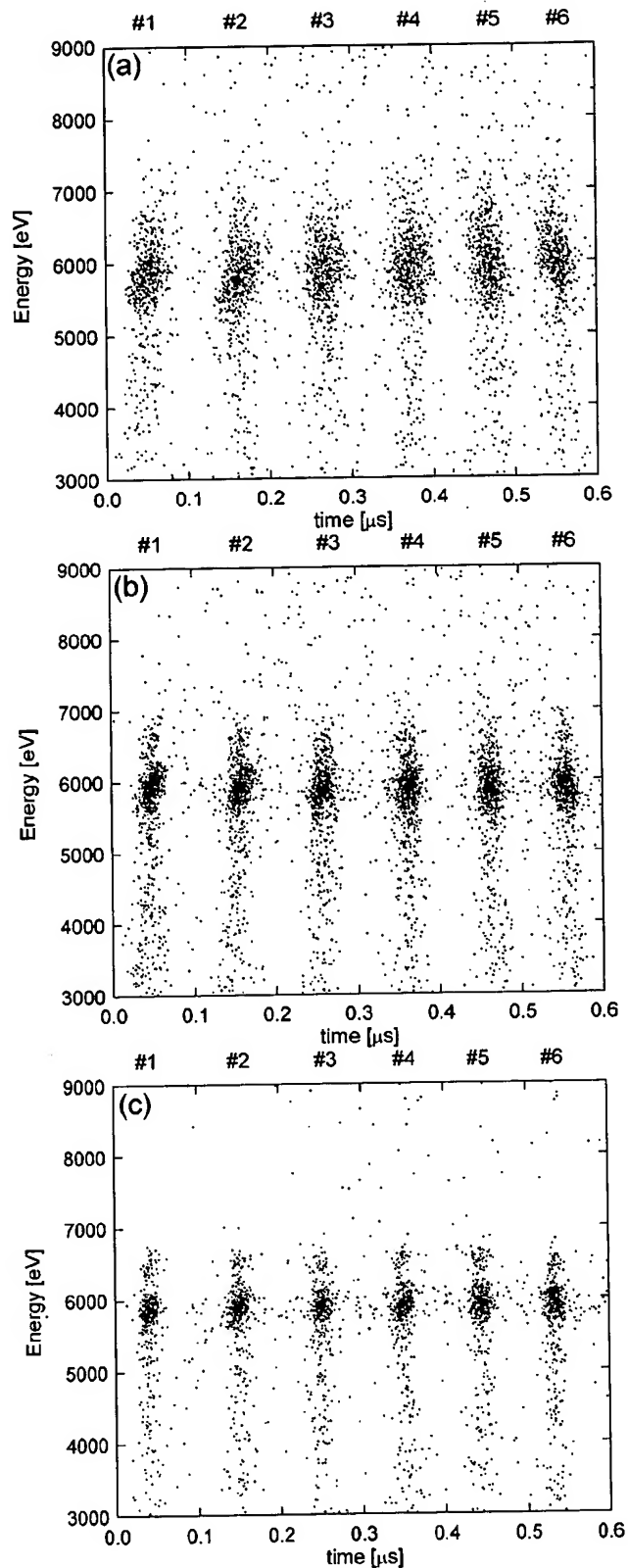


Fig. 2. Scatter plot energy versus drift time of the X-rays of a  $^{55}\text{Fe}$  source collected by a column of the CDD. The measurement was carried out at room temperature. The clusters have been labeled with the corresponding pixel numbers. (a) 10-kHz frame rate (integration time 90  $\mu$ s), (b) 30-kHz frame rate (integration time 30  $\mu$ s), and (c) 100-kHz frame rate (integration time 9  $\mu$ s).

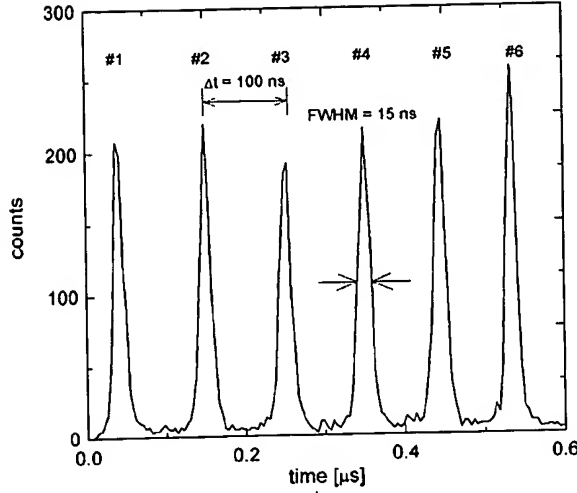


Fig. 3. Distribution of the events of Fig. 2(c) along the drift time (equivalent to the drift coordinate). The pixel number is indicated close to the corresponding peak.

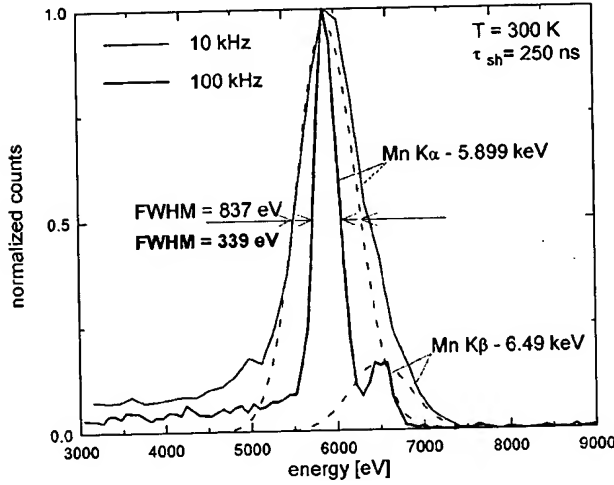


Fig. 4. Distribution of the events of Fig. 2(a) and (c) along the energy. The detector operating temperature is  $T = 300$  K and the shaping time is  $\tau_{sh} = 250$  ns.

### III. ANALYSIS OF THE ENERGY RESOLUTION

The readout noise can be expressed in terms of the ENC as

$$ENC^2 = ENC_{el}^2 + ENC_{parallel}^2 + ENC_{dig}^2. \quad (1)$$

The noise analysis shows that the contributions are from the noise of the electronic chain ( $ENC_{el} = 20$  electrons rms), the quantization noise of the 8-bit digitizer ( $ENC_{dig} = 12$  electrons rms), and from the parallel noise ( $ENC_{parallel}$ ) due to the leakage current (about 40 pA/channel) integrated in the pixels during the integration time.

We can model the noise contribution due to the integrated leakage charge as follows. During the integration mode, the leakage current fills the potential wells of the pixels. The average value of the leakage charge in each pixel is equal to

$$Q_L = J_L \cdot A_{pixel} \cdot T_{int} \quad (2)$$

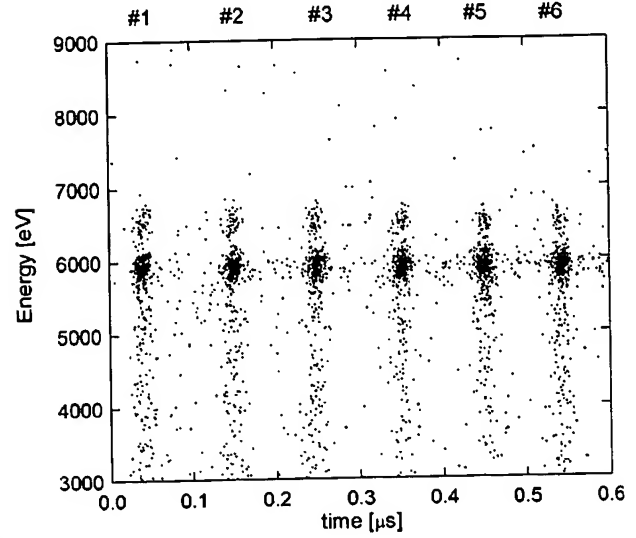


Fig. 5. Scatter plot energy versus drift time of the X-rays of a  $^{55}\text{Fe}$  source collected by a column of the CDD at 100-kHz frame frequency. The integration time was set to  $6.7 \mu\text{s}$  and the readout time to  $3.3 \mu\text{s}$ .

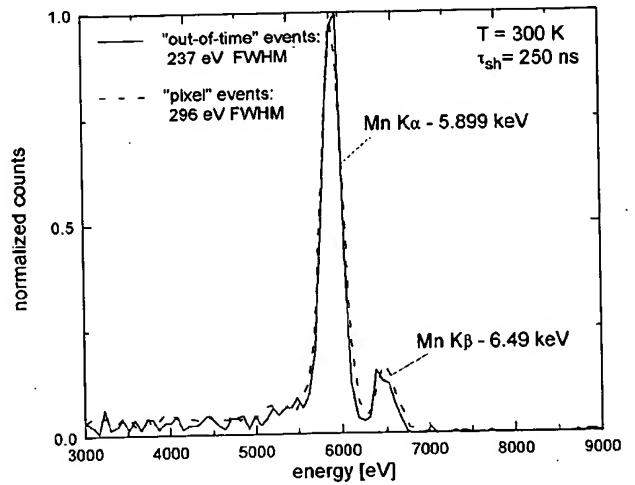


Fig. 6. Comparison of the distribution of the events of Fig. 5 along the energy and of the out-of-time events. The detector operating temperature is  $T = 300$  K and the shaping time is  $\tau_{sh} = 250$  ns.

where

- $J_L$  leakage current per unit area;
- $A_{pixel}$  area of one pixel;
- $T_{int}$  duration of the integration time.

After the transition to the drift mode, the charges  $Q_L$  are released by the pixels and start moving toward the collecting anode. The motion of the integrated charge pulses gives rise to a current pulse that lasts for a time equal to the drift time from the last pixel ( $T_{drift_{max}}$ ) and of average amplitude

$$I_{L,int} = \frac{N_{pixel} \cdot Q_L}{T_{drift_{max}}} = \frac{J_L \cdot N_{pixel} \cdot A_{pixel} \cdot T_{int}}{T_{drift_{max}}} \approx I_L \frac{T_{int}}{T_{drift_{max}}} \quad (3)$$

where  $N_{pixel}$  is the number of pixels in a column and  $I_L$  is the leakage current at the anode when the CDD is operated in

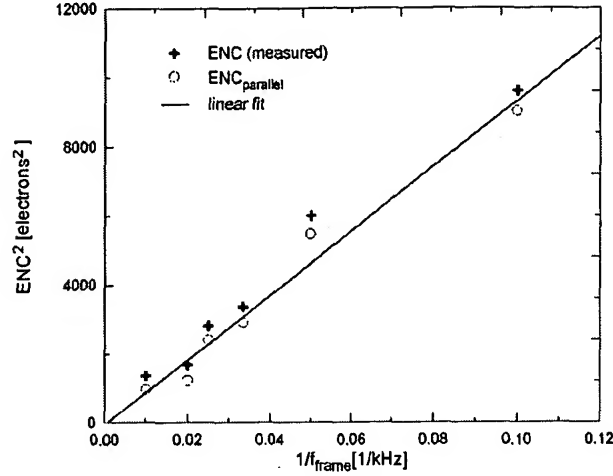


Fig. 7. Measured  $ENC^2$  as a function of the inverse of the frame rate. The derived contribution of the parallel noise is also shown.

free-running. The last equality is a slight overestimation due to the fact that  $I_L$  also includes the leakage current generated in the anode region. As the drift time from the last pixel ( $T_{drift,max} \cong 0.7 \mu s$ ) is greater than the shaping time ( $0.25 \mu s$ ), we can estimate the parallel noise contribution ( $ENC_{parallel}^2$ ) to the  $ENC^2$  as follows:

$$ENC_{parallel}^2 = A_3 q I_L \left[ 1 + \frac{T_{int}}{T_{drift,max}} \right] \tau_{sh} \quad (4)$$

where

- $A_3$  shape factor of the filter for parallel noise contribution;
- $q$  electron charge;
- $\tau_{sh}$  time constant of the filter.

A first confirmation of the proposed model is given by comparing the energy resolution at the Mn  $K\alpha$  line of the events collected during the integration phase with one of the so-called out-of-time events (i.e., the events hitting the detector during the readout phase and whose position of incidence cannot be determined). The two spectra are compared in Fig. 6 for a frame frequency of 100 kHz and a duration of the integration phase of  $6.7 \mu s$ . We considered only the out-of-time events hitting the detector in the last  $0.3 \mu s$  of the readout phase when the leakage current pulse of amplitude  $I_{L,int}$  has expired. The resolution at the  $K\alpha$  line is 237 eV FWHM equal to the resolution achievable with the controlled-drift detector operated in free-running, that is, always in the readout phase.

In Fig. 7, the measured  $ENC^2$  is reported as a function of the inverse of the frame rate. Subtracting quadratically the known contributions of the noise of the electronic chain and the quantization noise from the measured ENC, we calculated the parallel noise contribution. At 10-kHz frame rate, the parallel noise contribution is of 95 electrons, while at 100-kHz frame rate the parallel noise contribution reduces to 31 electrons. From the slope of the fit, we get  $I_L = 40$  pA. The plot of  $ENC^2$  as a function of the frame frequency shows good agreement between model and experiment. The spread of the measured points is also related to the approximated energy-voltage calibration factor.

As verified, the increase in the frame rate allows us to reduce significantly the dominant noise contribution of the integrated

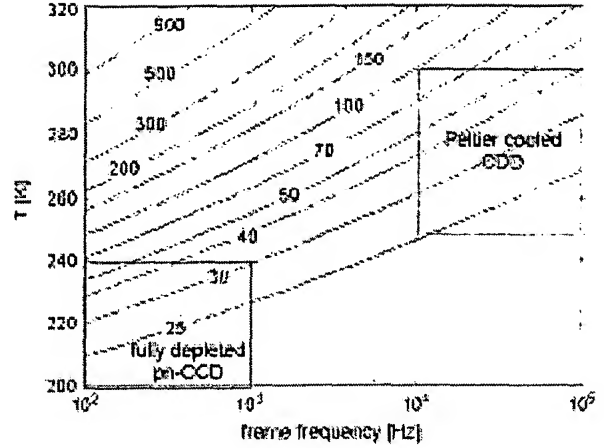


Fig. 8. Contour plot of the achievable energy resolution in terms of ENC as a function of the detector working temperature and of the frame frequency. The ratio between integration time and readout time is set equal to nine.

leakage charge. A well-known way to reduce the thermally generated current is to cool down the detector. In the case of the fully depleted pn-CDDs [3], the only way to reach maximum performances is to cool down the detector, as the duration of the readout time is typically limited to the millisecond range.

The achievable energy resolution, expressed by (1), has been estimated as a function of the operating temperature and of the frame rate. To this end, we assumed that the temperature dependence of the detector leakage current is the same as  $n_i^2(T)$  (where  $n_i(T)$  is the intrinsic carrier density at temperature  $T$ ) while the noise contribution of the front-end electronics and of the digitizer was considered constant. Neglecting the increase of the JFET transconductance at lower temperatures leads to a pessimistic estimate of the energy resolution. The ratio between integration time and readout time is set equal to nine. The equiresolution lines of the estimated ENC in the plane (frame frequency, temperature) are shown in Fig. 8.

#### IV. CONCLUSION

In this paper, we presented the first extended characterization of the position-sensing and spectroscopic capabilities of the CDD. One-dimensional images of a  $^{55}Fe$  have been acquired with the CDD operated at room temperature at different frame frequencies up to 100 kHz. The achieved energy resolution at the Mn  $K\alpha$  line and at 100-kHz frame frequency is 339 eV FWHM. The detailed noise analysis that has been presented shows that a dominant contribution to the energy resolution is that of parallel noise. Moreover, the use of a digitizer with a number of bits greater than eight will practically cancel the quantization noise contribution. The possibility to operate the detector at higher frame rates (i.e., shorter integration times) is equivalent to virtually cooling the detector. As a result, the room-temperature energy resolution approaches the limiting value, obtainable only at cryogenic temperatures if the detector is operated at lower frame rates.

We can expect to achieve energy resolutions close to present state-of-the-art X-ray imagers with more compact Peltier-cooled controlled-drift detector systems.

## ACKNOWLEDGMENT

The authors gratefully acknowledge many stimulating discussions with E. Gatti.

## REFERENCES

- [1] A. Castoldi, C. Guazzoni, A. Longoni, E. Gatti, P. Rehak, and L. Strüder, "Conception and design criteria of a novel silicon device for the measurement of position and energy of X-rays," *IEEE Trans. Nucl. Sci.*, vol. 44, pp. 1724–1732, 1997.
- [2] A. Castoldi, E. Gatti, C. Guazzoni, A. Longoni, P. Rehak, and L. Strüder, "The controlled-drift detector," *Nucl. Instrum. Meth.*, vol. A439, pp. 519–528, 2000.
- [3] L. Strüder, H. Bräuninger, U. Briel, R. Hartmann, G. Hartner, D. Hauff, N. Krause, B. Maier, N. Meidinger, E. Pfeffermann, M. Popp, C. Reppin, R. Richter, D. Stöter, J. Trümper, U. Weber, P. Höll, J. Kemmer, H. Soltan, A. Viehl, and C. v. Zanthier, "A 36 cm<sup>2</sup> large monolithic pn-charge coupled device X-ray detector for the European XMM satellite mission," *Rev. Sci. Instrum.*, vol. 68, pp. 4271–4274, 1997.



## Comparison of 5 and 10 mm thick $\text{HgI}_2$ pixelated $\gamma$ -ray spectrometers

James E. Bacia\*, Zhong He

*University of Michigan, Ann Arbor, MI 48109, USA*

### Abstract

$\text{HgI}_2$  detectors fabricated with pixelated anodes were tested as potential room temperature spectrometers. Spectra were obtained with 5 and 10 mm thick devices, and their results were compared. The 5 mm thick devices showed some effect of the anode weighting potential, while the 10 mm thick devices showed the effects of charge diffusion/sharing and electron trapping. A resolution near 1.4% FWHM using a  $^{137}\text{Cs}$  source was achieved after correcting for the interaction depth within the detector. The resolution from individual depths was as low as approximately 1.1% FWHM.  
© 2003 Elsevier Science B.V. All rights reserved.

PACS: 29.30; 29.40.Wk

Keywords: Mercuric iodide; Room temperature; Compound semiconductor;  $\gamma$ -ray detectors

### 1. Introduction

Mercuric iodide ( $\text{HgI}_2$ ) crystals are being investigated as a potential  $\gamma$ -ray spectrometer that can operate at room temperature. However, like most compound semiconductor  $\gamma$ -ray spectrometer materials,  $\text{HgI}_2$  suffers from poor charge transport characteristics. Despite the fact that  $\text{HgI}_2$  has a wide band gap, high average atomic number, and a high density, the crystals suffer from low electron and hole mobility, significant hole trapping, and material non-uniformity. For these reasons,  $\text{HgI}_2$  spectrometers have been limited to a thickness less than 3 mm. To improve the spectroscopic performance of thicker  $\text{HgI}_2$

detectors, one must reduce the depth dependence of the generated pulse from a  $\gamma$ -ray interaction event common to these materials.

The use of single-polarity charge sensing was implemented in order to overcome the severe hole trapping present in wide band gap semiconductor detectors, including  $\text{HgI}_2$ . The introduction of pixelated anodes to  $\text{CdZnTe}$  [1,2] and  $\text{HgI}_2$  [3] showed that the resolution of wide band gap semiconductor detectors can be dramatically improved compared to standard planar electrode configuration. By simultaneously measuring the signal from the planar cathode and anode pixels, the interaction depth [4] can be obtained by calculating the ratio of the induced charge on each electrode.

In this paper, we present and compare spectroscopic results from 5 and 10 mm thick  $\text{HgI}_2$  detectors. Both raw and depth-corrected spectra

\*Corresponding author. Tel.: +1-734-936-0127; fax: +1-734-763-4540.

E-mail address: [jimbar@umich.edu](mailto:jimbar@umich.edu) (J.E. Bacia).

are presented, along with a comparison of the peak position as a function of depth of interaction.

## 2. Detector description and setup

The anode pixel configuration used in this work is shown in Fig. 1. The four small pixels are surrounded on all sides by a large anode plate. The area of each pixel is  $\sim 1 \text{ mm}^2$  and is comprised of palladium. When the cathode is negatively biased, electrons moving toward the anode surface induce charge on the pixels. The induced charge on a pixel is determined mainly by the movement and collection of electrons underneath each pixel. The signal produced by the anode pixel is only slightly dependent upon the distance traveled by the electrons, and is not significantly affected by hole movement.

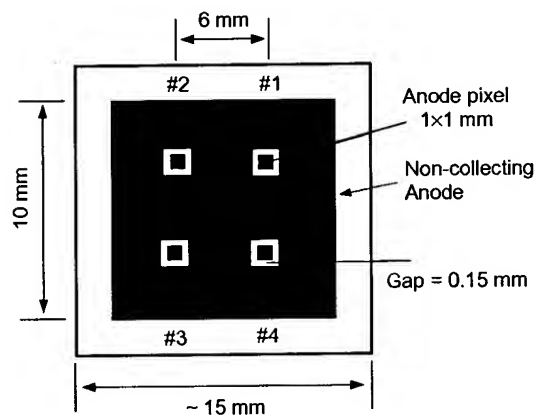


Fig. 1. Top: view of the  $\text{HgI}_2$  anode configuration. Bottom: cross-sectional view of the crystal. The lines under the pixels represent the region of the detector where the majority of the induced charge on the anode is produced.

The detector electrodes are connected to Amp-Tek [5] A250 charge-sensitive preamplifiers, which are connected to standard NIM shaping amplifiers for pulse shaping and amplification purposes. The signals are fed into peak-hold circuitry to hold the peak of the shaped pulse for a sufficiently long time before the ADC samples the pulse amplitude. The signals are analyzed by programs produced using LabVIEW™ and Matlab® software.

## 3. Results

### 3.1. 5 mm thick detectors

The majority of the data from 5 to 6 mm thick detectors have been described previously [6]. These detectors had resolutions near 2.1% FWHM at 662 keV after correcting for the interaction depth. Interaction depth is broken up into 20 thin strips known as the “depth index.” For example, a depth index of 1 would indicate events near the anode surface, while a depth index of 20 indicates events near the cathode surface. The resolution obtained at individual depth indices reached 1.6% FWHM (Fig. 2). The resolution of the spectra was independent of the depth index; however, spectral

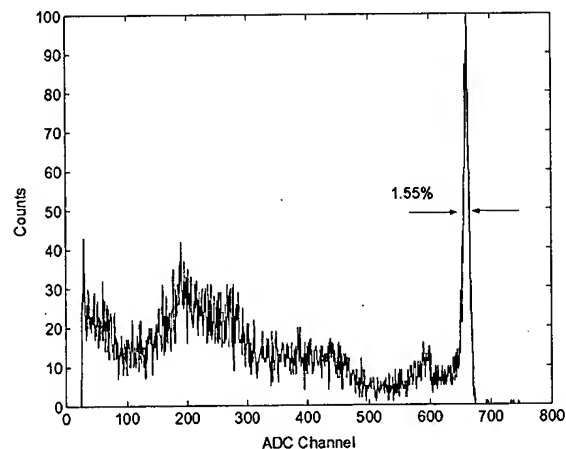


Fig. 2.  $^{137}\text{Cs}$  spectrum collected over 22 h from an individual depth of a 5.9 mm thick detector (Pixel #2) biased at  $-1500 \text{ V}$  and using a shaping time of  $4 \mu\text{s}$ . The resolution of the 662 keV  $\gamma$ -ray was 1.55%. The events selected here are from interactions near the middle of the detector.

resolution from events near the electrodes (anode or cathode) degraded to 2.3–3.7% FWHM. Poor resolution near the anode was expected because, in this region, the induced charge (weighting potential) has a steep slope. Thus, the recorded pulse can be highly dependent on the interaction depth near the anode and on the induced charge produced by the small amount of hole movement present in these detectors. For events near the cathode, the degradation in energy resolution was due to electron trapping, charge sharing between the anode pixel and the non-collecting anode, and material non-uniformity effects.

### 3.2. 10 mm thick detectors

Fig. 3 is an example spectrum collected over the same time frame as the 5 mm devices. The resolution of the spectrum was approximately 3% FWHM at 662 keV prior to correcting for interaction depth, and improved to 1.4% FWHM after depth correction. Resolutions as low as 1.0–1.1% FWHM can be observed when analyzing the spectra from individual depths (Fig. 4). The lack of dependence on hole movement and the dependence of peak position on interaction depth were also seen in the 10 mm detector.

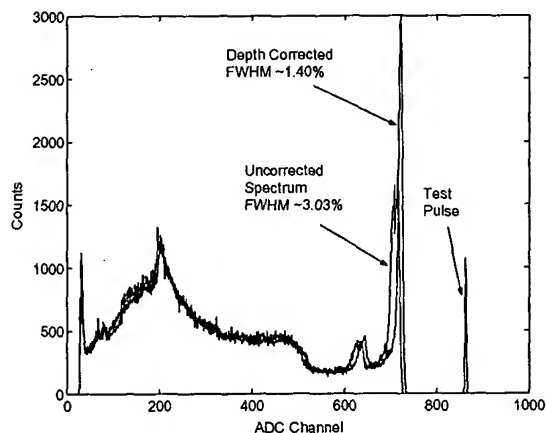


Fig. 3.  $^{137}\text{Cs}$  spectrum collected over 22 h from a 10 mm thick detector (Pixel #2) biased at  $-2500$  V and using a shaping time of  $8\text{ }\mu\text{s}$ . The electronic noise of the system was approximately  $2.8\text{ keV}$ . This value was consistent for all pixels tested.

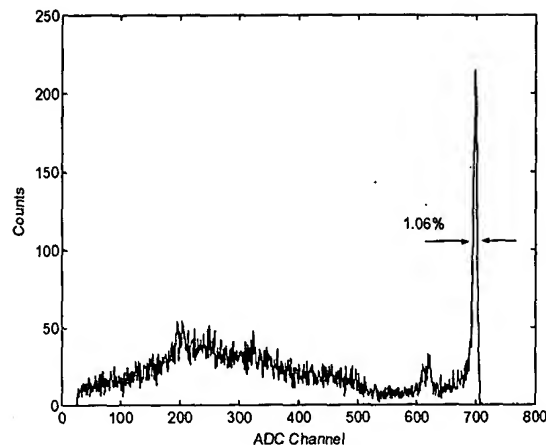


Fig. 4.  $^{137}\text{Cs}$  spectrum collected over 22 h from an individual depth of a 10 mm thick detector (Pixel #2) biased at  $-2500$  V and using a shaping time of  $4\text{ }\mu\text{s}$ . The resolution of the  $662\text{ keV}$   $\gamma$ -ray was 1.06%. The depth index of this spectra was 10, which corresponds to  $\gamma$ -ray interactions from the middle of the detector (i.e., 5 mm from the cathode or anode surface).

### 4. Discussion

It is important to note that differences in the weighting potential, electron trapping, and charge sharing between anode pixels can have a significant effect on the spectra between 5 and 10 mm thick  $\text{HgI}_2$  detectors. For thinner pixelated detectors, there will be a larger dependence on depth as electrons traverse the detector. This is shown in Fig. 5. The slope of the weighting potential throughout the majority of the thickness of the detector is slightly larger for 5 mm detectors. The non-zero slope in the bulk of the detector causes the induced signal to have a slight depth dependence. This results in a variation of photopeak position as a function of interaction depth. This effect can be seen when comparing peak position data with expected results (Fig. 6).

When comparing the peak position as a function of depth index between 5 and 10 mm thick detectors, a number of features can be distinguished. The 5 mm peak positions tended to lie below the expected curve for nearly all depth indices. This indicates that there was a more severe depth dependence on the induced charge than what was expected. The assumptions on weighting

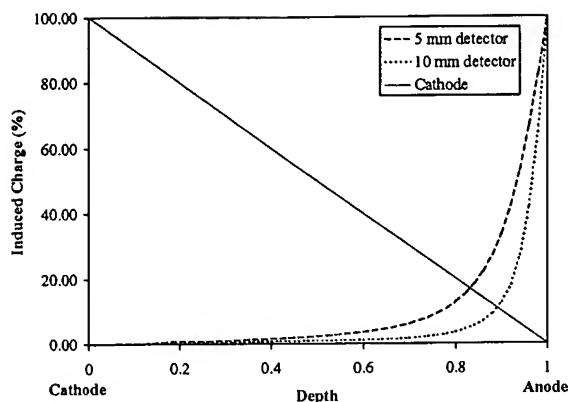


Fig. 5. Weighting potential versus normalized depth for 5 and 10 mm thick  $\text{HgI}_2$  pixelated anodes. The weighting potential for the planar cathode is also presented for reference.

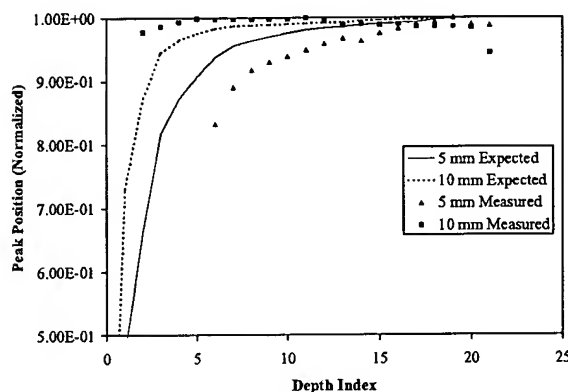


Fig. 6. Normalized peak position as a function of depth index.

potential (such as material uniformity) may not be entirely correct in this case [7]. A more severe depth dependence would adversely affect the overall resolution even with depth correction. Despite its advantages, depth correction cannot overcome the finite difference in the weighting potential within an individual depth (or voxel) itself.

The number of depths that contained a clear photopeak was larger for 10 mm thick detector as a result of the weighting potential. While the 10 mm measurements agree quite well with expectations, the measured data tends to be slightly higher for events near the anode (depth index 3–7) and slightly lower than expected for events near the

cathode (depth index 15–20). The slightly higher induced charge could be due to a small amount of hole movement within the detector. The decrease in induced charge from  $\gamma$ -ray events near the cathode could be due to electron trapping and charge sharing.

## 5. Conclusion

$\text{HgI}_2$  detectors of 5–10 mm thickness with pixelated anodes have been tested as potential room temperature  $\gamma$ -ray spectrometers. Since hole collection is unnecessary, relatively low electric fields and short shaping times were used. By using pixelated anodes and depth sensing and correction techniques, the resolution of individual pixels can be less than 2% FWHM when using a  $^{137}\text{Cs}$  source. These detectors show no significant polarization effects resulting in the degradation of resolution. However, the 10 mm results showed the effects of charge trapping and charge sharing that degraded the signal from events near the cathode. If these effects can be reduced, the detector performance (resolution and photopeak efficiency) should improve.

## Acknowledgements

This work was supported by Constellation Technologies, Largo, FL.

## References

- [1] H.H. Barrett, Phys. Rev. Lett. 75 (1995) 156.
- [2] Z. He, W. Li, G.F. Knoll, D.K. Wehe, J. Berry, C.M. Stahle, Nucl. Instr. and Meth. A 422 (1999) 173.
- [3] Z. He, R.D. Vigil, Nucl. Instr. and Meth. A 492 (2002) 387.
- [4] Z. He, G.F. Knoll, D.K. Wehe, R. Rojeski, C.H. Mastrangelo, M. Hammig, C. Barrett, A. Uritani, Nucl. Instr. and Meth. A 380 (1996) 228.
- [5] Amptek, Inc., 6 Angelo Drive, Bedford, MA 01730, USA.
- [6] J.E. Baciak, Z. He, R.P. DeVito, IEEE Trans. Nucl. Sci. NS-49 (3) (2002) 1264.
- [7] Z. He, Nucl. Instr. and Meth. A 365 (1995) 572.